

Non-Hermitian chiral phononics through optomechanically induced squeezing

<https://doi.org/10.1038/s41586-022-04609-0>

Javier del Pino^{1,2,3}✉, Jesse J. Slim^{1,3} & Ewold Verhagen¹✉

Received: 19 October 2021

Accepted: 4 March 2022

Published online: 1 June 2022

 Check for updates

Imposing chirality on a physical system engenders unconventional energy flow and responses, such as the Aharonov–Bohm effect¹ and the topological quantum Hall phase for electrons in a symmetry-breaking magnetic field. Recently, great interest has arisen in combining that principle with broken Hermiticity to explore novel topological phases and applications^{2–16}. Here we report phononic states with unique symmetries and dynamics that are formed when combining the controlled breaking of time-reversal symmetry with non-Hermitian dynamics. Both of these are induced through time-modulated radiation pressure forces in small nano-optomechanical networks. We observe chiral energy flow among mechanical resonators in a synthetic dimension and Aharonov–Bohm tuning of their eigenmodes. Introducing particle-non-conserving squeezing interactions, we observe a non-Hermitian Aharonov–Bohm effect in ring-shaped networks in which mechanical quasiparticles experience parametric gain. The resulting complex mode spectra indicate flux-tuning of squeezing, exceptional points, instabilities and unidirectional phononic amplification. This rich phenomenology points the way to exploring new non-Hermitian topological bosonic phases and applications in sensing and transport that exploit spatiotemporal symmetry breaking.

From the Zeeman to the quantum Hall effect, magnetic fields biasing electronic systems alter their spectrum and imprint chirality on their eigenstates. Nonreciprocal interference underlies these phenomena, as electrons travelling along a closed path gain a phase proportional to the enclosed magnetic flux that depends on direction—evidencing broken time-reversal (\mathcal{T}) symmetry. Such geometrical phases¹ and the resulting synthetic magnetism were recently brought to bosonic systems in photonics, acoustics, and cold atoms to explore nonreciprocal functionality^{17–20} and various topological insulators^{21,22}.

In a parallel, largely unconnected development, researchers turned to non-Hermitian systems including parity–time (PT)-symmetric systems, which feature dynamical phase transitions linked to spectral singularities such as exceptional points^{23,24}. Here, controlled gain and loss lead to unique eigenmode symmetries and tuning of complex eigenfrequencies ϵ . Bosonic systems form the natural realm for these phenomena, with lasing and self-oscillation ubiquitous in photonics and mechanics. In particular, bosonic squeezing is described by Hamiltonians that do not conserve excitation number, and engender distinct phases showing stable or unboundedly growing dynamics^{25,26}.

Very recently, the combination of topology and non-Hermiticity attracted strong interest^{2,3}. Tailoring gain and loss in topological insulators showed lasing into protected states^{6,7,12} and topological phase transitions⁸. In principle, states with symmetries, dynamics, and spectra that are altogether different from Hermitian chiral systems are expected^{4,5}. Indeed, various non-Hermitian topological phases were predicted, with associated chirally amplified and unstable edge modes^{9–11}, quadrature-dependent chiral transport^{27,28} and anomalous

bulk-boundary correspondence with extreme sensitivity to boundary conditions^{2,13–16}. However, the rich combination of squeezing interactions and geometrical phases remained experimentally unexplored so far.

Here we demonstrate Aharonov–Bohm interference and chirality of nanomechanical states in multi-resonator networks where both \mathcal{T} -symmetry-breaking geometrical phases and non-Hermiticity are induced through radiation pressure. Because suitable laser drives stimulate frequency-converting transitions, optomechanical control²⁹ allows parametric amplification and synthetic magnetism for photons^{18,19} and phonons^{30,31}. We combine both here, using squeezing interactions in addition to particle-conserving interactions to create non-Hermitian dynamics without dissipation^{25,32} and uncover new geometrical phases. Using light to sensitively actuate and detect nanomechanical motion, we reveal the unique effects of this merger on chiral transport, dynamical phases and squeezing, and actively control them in space and time.

Phononic circulation

We first induce phononic chirality by breaking \mathcal{T} symmetry in a network with Hermitian closed-system dynamics, henceforth simply called Hermitian. We disregard the small intrinsic mechanical dissipation in the most basic description of the systems, while including it in all relevant calculations (Methods). A sliced photonic-crystal nanobeam³¹ supports multiple non-degenerate MHz-frequency flexural mechanical modes coupled to the optical field of a nanocavity. Each mode

¹Center for Nanophotonics, AMOLF, Amsterdam, the Netherlands. ²Institute for Theoretical Physics, ETH Zürich, Zurich, Switzerland. ³These authors contributed equally: Javier del Pino, Jesse J. Slim.
✉e-mail: jdelpino@phys.ethz.ch; verhagen@amolf.nl

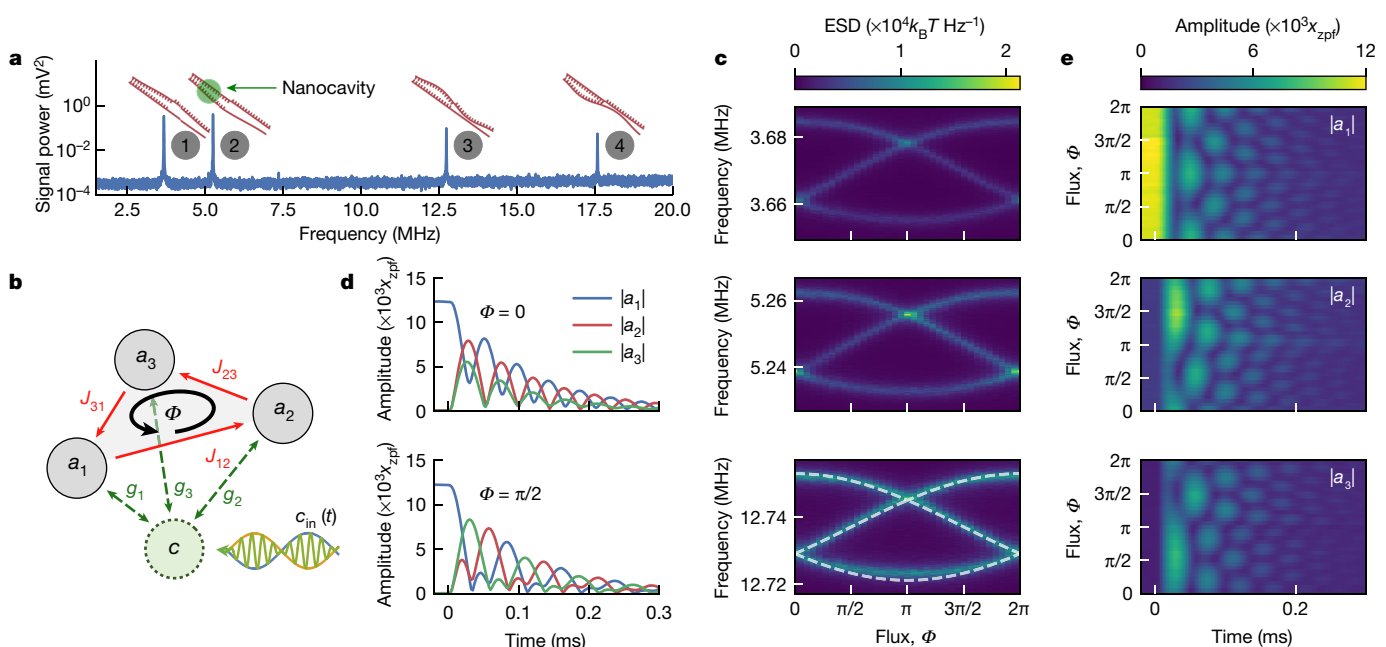


Fig. 1 | Aharonov–Bohm interference in a Hermitian nano-optomechanical network. **a**, Thermomechanical fluctuation spectrum of the sliced photonic crystal nanobeam, imprinted on a laser reflected from a nanocavity with linewidth $\kappa/(2\pi) = 320$ GHz. Resonances forming a synthetic dimension correspond to mechanical flexural modes at frequencies $\omega_i/(2\pi) = \{3.7, 5.3, 12.8, 17.6\}$ MHz with loss rates $\gamma_i/(2\pi) \approx 1–4$ kHz and estimated vacuum optomechanical coupling rates $g_0^{(i)}/(2\pi) = \{5.3, 5.9, 3.3, 3.1\}$ MHz. **b**, The modulated cavity field c couples the three lowest-frequency resonators in a loop with rates $J_{ij}/(2\pi) = 8$ kHz and Peierls phases φ_{ij} , adding up to flux Φ . These coupling strengths are achieved with modulation depths c_m between 0.32 and 0.42, at mean photon number $\bar{n}_c \approx 343$. **c**, Thermomechanical noise spectra imprinted on the detection laser around each resonator's sideband versus flux.

Hybridized Floquet modes tune with synthetic flux. ESD, energy spectral density. **d**, Time evolution of resonator amplitudes $|\langle a_i \rangle| = |a_i|$ for unbroken ($\Phi = 0$) and broken ($\Phi = \pi/2$) \mathcal{T} symmetry. Resonator a_1 is coherently driven until $t = 0$ ms through resonantly modulated radiation pressure, when excitation is stopped and modulation tones implementing the couplings are established. **e**, Time evolution of resonator amplitudes for varying flux, showing crossover from helical to non-helical transport through an intermediate regime with generally aperiodic dynamics, and reversal of chirality with flux sign ($\Phi \mapsto -\Phi$). For reference, the optomechanical coupling routinely reaches experimental cooperativities $C_{ij} = 4J_{ij}^2/(\gamma_i\gamma_j) > 80$, allowing two-mode transfer efficiencies of approximately 70% (Extended Data Fig. 1).

(‘resonator’) i changes the cavity frequency by $g_0^{(i)}x_i$ through displacement x_i (normalized to the zero-point amplitude x_{zpf}) and experiences a force proportional to $g_0^{(i)}n_c$, with $g_0^{(i)}$ the vacuum optomechanical coupling rate and n_c the intracavity photon number. Figure 1a shows distinct mechanical resonances in the thermomechanical noise spectrum, read out as modulations of a detuned probe laser reflected from the cavity (Methods).

Although the (uncoupled) mechanical resonators have well separated eigenfrequencies ω_i , interactions are established by temporal modulation of the intensity of a control laser detuned from cavity resonance. For optimal laser detuning $\Delta = -\kappa/(2\sqrt{3})$, with cavity decay rate κ , mechanical displacement modulates the intracavity intensity instantaneously at phononic timescales ($\kappa \gg \omega_i$). Mixing of a control laser intensity modulation at the difference frequency $\omega_j - \omega_i$ of resonators i and j with the radiation pressure force sideband of resonator i creates a sideband at ω_j . The resulting ‘cross-mode optical spring effect’³¹ induces particle-conserving beamsplitter coupling between the resonators at rate $J_{ij} = c_m g_i g_j 4/(\Delta^2 + \kappa^2/4)$, with laser-enhanced optomechanical coupling rate $g_i = g_0^{(i)}\sqrt{\bar{n}_c}$ scaling with average cavity population \bar{n}_c and modulation depth c_m (Methods).

Three resonators are coupled in a ring network by simultaneously applying three modulation tones (Fig. 1b). Describing the resonators by their annihilation operators a_i in frames rotating at ω_i , the phonon-number-preserving Hamiltonian for this ‘beamsplitter trimer’ (BST) reads:

$$H_{\text{BST}} = \sum_{i=1, j \neq i}^3 J_{ij} e^{-i\varphi_{ij}} a_i^\dagger a_j, \quad \varphi_{ji} = -\varphi_{ij}, \quad (1)$$

without intrinsic dissipation. This Hamiltonian importantly imprints the modulation phase φ_{ij} in a nonreciprocal fashion on phonons transferred along the loop—precisely like the Peierls phase imprinted by a magnetic vector potential³¹. The gauge-invariant geometrical phase $\Phi = \varphi_{12} + \varphi_{23} + \varphi_{31}$ around the loop then represents a synthetic flux threading the resonator plaquette.

Setting equal $J_{ij} = J$, the Hamiltonian (equation (1)) is translationally invariant in a gauge with equal Peierls phases, and therefore diagonal in the discrete momentum basis $\tilde{a}_k = \sum_{j=1}^3 e^{-i2\pi k j / 3} a_j / \sqrt{3}$ for $k = \{-1, 0, 1\}$. Through Aharonov–Bohm interference along the loop, the enclosed flux shifts the eigenfrequencies $\epsilon_k = 2/\cos((2\pi k + \Phi)/3)$. Figure 1c reveals these states in the thermomechanical spectrum, for each resonance splits into a (Floquet) triplet owing to strong coupling $J > \gamma_i$ with mechanical damping rates γ_i . This demonstration of nanomechanical flux-tuning is paralleled in the spectra of quantum rings under magnetic fields³³. We note that with homogeneous dissipation ($\gamma_i = \gamma$) closed-system behaviour is recovered for transformed modes $a'_i = a_i e^{i\gamma t/2}$ (ref. ²⁴).

The flux-tuning manifests Aharonov–Bohm interference over a given rotation—the mechanism ultimately responsible for chirality of quantum Hall edge states²² and nonreciprocal dynamics³³. Figure 1d, e shows evolution of a mechanical excitation with chirality controlled by the flux. For $\Phi \in \{0, \pi\}$, the beamsplitter trimer is time-reversal symmetric (Methods) and energy simultaneously hops to both other resonators. Any other flux breaks \mathcal{T} symmetry, lifting the degeneracy of opposite momentum eigenstates and enabling chiral energy transport, manifested for $\Phi = \pi/2$ ($\Phi = -\pi/2$) as a clockwise (counter-clockwise) circulation.

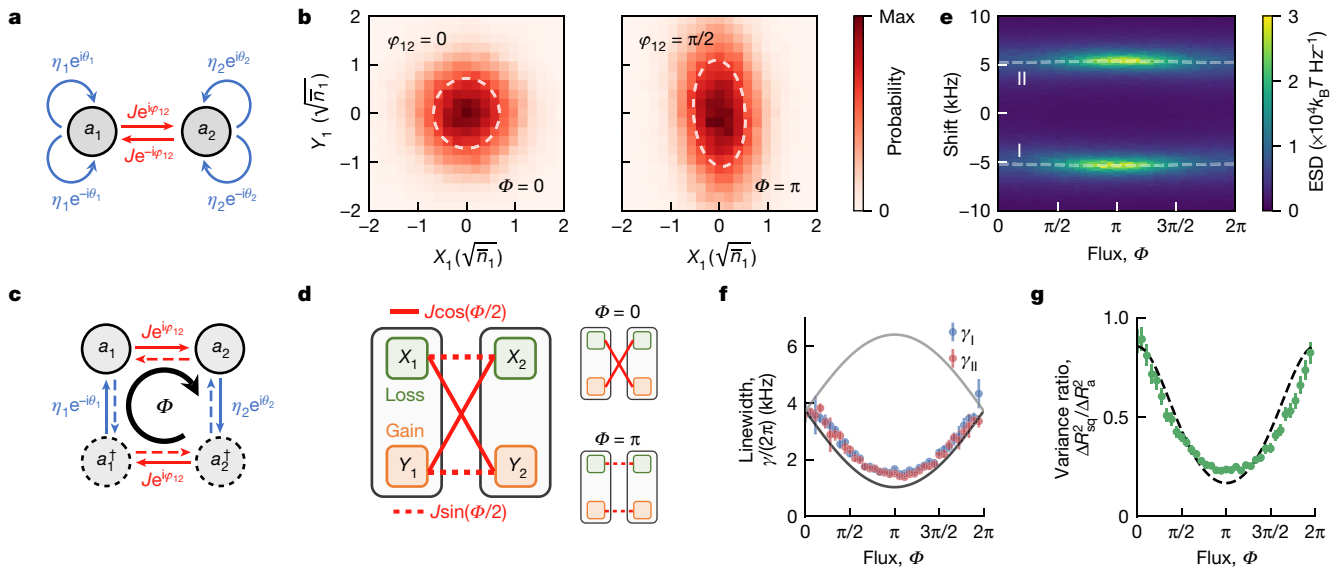


Fig. 2 | Aharonov–Bohm interference along non-Hermitian squeezing loops. **a**, The squeezing dimer encompasses two resonators driven at $2\omega_1$ and $\omega_2 - \omega_1$. These introduce single-mode nanomechanical squeezing (blue self-loops) and beamsplitter coupling (red). We use the modes labelled (3) and (4) in Fig. 1a as resonators 1 and 2, respectively. **b**, Histograms of the steady-state phase-space distribution of resonator 1 for different beamsplitter Peierls phase φ_{12} , showing its effect on thermomechanical squeezing. Dashed ellipses depict the standard deviation of the principal components of the quadrature covariance matrix. Here $\theta_1 = \theta_2 = \pi/2$. **c**, Graph associated with the Hamiltonian matrix (equation (3)), unwrapping self-loops in **a** over particles (annihilated by a_i) and holes (annihilated by a_i^\dagger). The clockwise loop is threaded by synthetic flux Φ , the counter-clockwise by $-\Phi$. **d**, Coupling diagram for resonator quadratures, where Φ controls the coupling between the squeezed (green) and anti-squeezed (orange) quadratures of the two resonators.

e, Thermomechanical spectra for the squeezing dimer around ω_1 . **f**, Sweeping flux continuously tunes the fitted apparent resonance linewidths $\gamma_{1,II}$ (blue and red circles), compared to the theoretical loss rate of the lowest-loss eigenfrequency of \mathcal{H}_{SD} (solid black). The other, higher loss rate is shown for reference (solid gray). **g**, Flux-dependent level of squeezing, measured as the ratio of the variances ΔR_{sq}^2 and ΔR_a^2 of the quadratures squeezed and anti-squeezed along the principal axes of the covariance matrix, respectively, in experiment (green) and theory (dashed, Supplementary Information section IIA, B). Here $J/(2\pi) = 5.37$ kHz, $\eta_1/(2\pi) = \eta_2/(2\pi) = 1.34$ kHz, and loss rates $\gamma_1/(2\pi) \approx \gamma_2/(2\pi) = 3.7$ kHz, equalized by optical tuning (Methods section ‘Resonator characterization’). Error bars in **g** are dominated by fitting (statistical) uncertainties, with a small contribution from control parameter fluctuations (Methods section ‘Error estimation’). ESD, energy spectral density.

Non-Hermitian Aharonov–Bohm effect

We thus demonstrated a chiral phononic circulator³⁴ using light-induced nanomechanical beamsplitter interactions, with scaling potential to topological lattices³¹. Still, vastly richer phenomenology is uncovered by introducing squeezing interactions in the nodes and links of the network, which were not considered in earlier work. We implement single-mode ($i=j$) or two-mode ($i \neq j$) mechanical squeezing by optical modulation at the sum frequency $\omega_i + \omega_j$. The Hamiltonian reads (Methods):

$$H^{sq} = \sum_{i,j} \frac{\eta_{ij}}{2} (e^{i\theta_{ij}} a_i a_j + e^{-i\theta_{ij}} a_i^\dagger a_j^\dagger), \quad (2)$$

with interaction strength $\eta_{ij} = c_m g_i g_j \Delta / (\Delta^2 + \kappa^2/4)$ and modulation phase θ_{ij} now imprinted on the creation or annihilation of phonon pairs. Squeezing angles θ_{ij} form a powerful control resource, as did the Peierls phases φ_{ij} previously. Indeed, spatially patterned squeezing yields anomalous pairing terms, enabling topological bosonic states unparalleled by their fermionic (for example, topological superconductor) counterparts and is essential for proposed topological amplifiers¹¹.

We first consider a ‘squeezing dimer’ (Fig. 2a) consisting of two resonators, each single-mode squeezed through $2\omega_i$ modulation, and coupled through driving at $\omega_2 - \omega_1$ (Hamiltonian, $H_{SD} = \eta_1 e^{i\theta_1} a_1^2/2 + \eta_2 e^{i\theta_2} a_2^2/2 + J e^{i\varphi_{12}} a_2^\dagger a_1 + H.c.$). Remarkably, we find that the level of squeezing of thermal fluctuations is not only determined by the interactions’ magnitude $\eta_{ii} J$, but also by their phases $\theta_{ii}, \varphi_{12}$. Figure 2b shows that single-mode squeezing is maximal when $\varphi_{12} = \pi/2$ and disappears when $\varphi_{12} \in \{0, \pi\}$ for $\theta_1 = \theta_2 = \pi/2$ and $\eta_1 = \eta_2 = \eta$.

We now show that this observation is associated with a non-Hermitian version of Aharonov–Bohm interference. Even though the coupled-mode picture Fig. 2a shows no plaquette, we can recognize a loop along which excitations experience a geometric phase when combining graph representation with Bogoliubov–de Gennes (BdG) formalism²⁶. Treating a_i and a_i^\dagger as separate degrees of freedom—‘particles’ and ‘holes’—and squeezing (equation (2)) as particle–hole conversion, this representation (Fig. 2c) reveals for the squeezing dimer a conjugate pair of superimposed loops in particle–hole space, threaded by gauge-invariant fluxes $\Phi = 2\varphi_{12} - \theta_1 + \theta_2$ and $-\Phi$. As these fluxes govern interference in the loop, they control the connection between the resonators’ quadratures (defined such that $X_i = (a_i + a_i^\dagger)/\sqrt{2}$ ($Y_i = i(a_i^\dagger - a_i)/\sqrt{2}$) are squeezed (anti-squeezed) for $j=0$): whereas $\Phi = \pi$ connects the squeezed quadrature X_1 to anti-squeezed quadrature Y_2 , $\Phi = 0$ connects squeezed quadrature X_1 to anti-squeezed quadrature Y_2 and vice versa, cancelling the overall squeezing (Fig. 2d, Methods).

Flux-controlled PT symmetry

This geometric phase again impacts normal mode frequencies. These are now generally complex—given by the eigenvalues of the BdG dynamical matrix \mathcal{H}_{SD} defining the closed-system equations of motion, $i\dot{\alpha} = \mathcal{H}_{SD}\alpha$ where $\alpha = (a_1, a_2, a_1^\dagger, a_2^\dagger)$ (Methods). Even without dissipation ($\gamma_i = 0$), squeezing makes \mathcal{H}_{SD} necessarily non-Hermitian, preserving only Σ_z -pseudo-Hermiticity ($\Sigma_z = \text{diag}(1, -1)$, $\mathcal{H}_{SD}^\dagger = \Sigma_z \mathcal{H}_{SD} \Sigma_z$) to satisfy bosonic commutation relations²⁶. Aharonov–Bohm-like interference in the BdG loop thus acquires a non-Hermitian character, where now both frequency and linewidth evolve with flux. In the

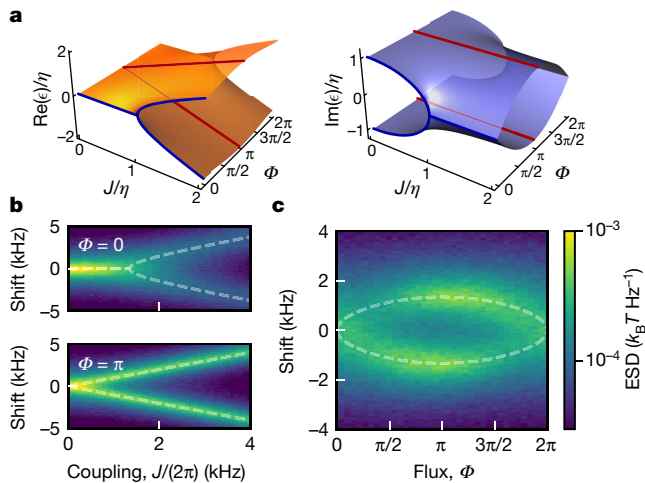


Fig. 3 | Flux control of non-Hermitian dynamical phases. **a**, Complex eigenfrequency surfaces of the squeezing dimer in J/η - Φ space for $\gamma_i = 0$, tuned by the non-Hermitian Aharonov–Bohm effect acting on its beamsplitter and squeezing links. For $\Phi \in \{0, 2\pi\}$ and $\eta = J$, \mathcal{PT} symmetry breaks spontaneously and the eigenspectrum coalesces into two second-order exceptional points. **b**, Fingerprints of complex degeneracies in the thermomechanical spectra for resonator 1 at $\eta/(2\pi) = 1.34$ kHz and varying J . Nonzero flux breaks $\mathcal{P}_{X,Y}\mathcal{T}$ symmetry explicitly, precluding exceptional points. **c**, Flux-tuned spectra for resonator 1 when $\eta/(2\pi) \approx \eta/(2\pi) = 1.34$ kHz, showing mode coalescence at the exceptional point at $\Phi \in \{0, 2\pi\}$. For **b** and **c**, theoretical eigenvalues $\text{Re}(\epsilon)$ are shown as dashed lines. In this experiment, resonances 3 and 4 have been used, employing dynamical backaction to equilibrate damping rates to $\gamma_i/(2\pi) = 3.7$ kHz (Methods). Fits of frequencies and linewidths are shown in Extended Data Fig. 2.

strongly coupled, dynamically stable regime ($J > \eta$, $2\eta < \gamma_i$, Fig. 2e, f), Φ strongly tunes the linewidth and thermal amplitude of the hybridized eigenmodes, in unison with squeezing (Fig. 2g). The squeezed and anti-squeezed partners recognized for $\Phi = \pi$ in Fig. 2d correspond to broad and narrow resonances, respectively³⁵, with the latter dominating the spectrum (Methods).

The complex eigenvalues define surfaces in J/η - Φ space (Fig. 3a) with varying degeneracy, indicating distinct dynamical phases. Their properties are appreciated by studying the dynamical matrix in the quadrature basis \mathcal{H}_{SD}^{XY} . For $\Phi = 0$, \mathcal{H}_{SD}^{XY} respects a $\mathcal{P}_{X,Y}\mathcal{T}$ symmetry for the two degenerate ‘quadrature dimers’ X_1Y_2 and X_2Y_1 (Fig. 2d), where $\mathcal{P}_{X,Y}$ exchanges $X_i \leftrightarrow Y_j$. We thus demonstrate \mathcal{PT} -symmetric physics by means of squeezing dynamics, instead of coupling to dissipative baths^{25,32}. The squeezing dimer features a pair of complex eigensurfaces, twofold degenerate in real and imaginary parts. The only effect of nonzero but equal dissipation is a uniform displacement of the dynamical matrix $\mathcal{H}_{SD}^{XY} \rightarrow \mathcal{H}_{SD}^{XY} - (i\gamma/2)\mathbb{I}$, where \mathbb{I} is the identity matrix (Methods), manifesting \mathcal{PT} symmetry in the basis $a'_i = a_i e^{i\pi t/2}$, that is, ‘passive’ \mathcal{PT} symmetry in the open system resulting from additional, local dissipation²⁴.

The thermomechanical spectra in Fig. 3b evidence the distinct dynamical phases. Along $\Phi = 0$, we recognize behaviour of the conventional \mathcal{PT} -symmetric dimer²⁴. Eigenmodes (hosted by quadrature dimers) respect \mathcal{PT} symmetry for $J > \eta$, with equal linewidths and splitting increasing with J . For $J < \eta$, \mathcal{PT} symmetry is spontaneously broken, with degenerate frequencies independent of J , while linewidths split (Extended Data Fig. 2). \mathcal{H}_{SD} becomes defective at a degenerate pair of second-order exceptional points (one per quadrature dimer), when $J = \eta$. Finite fluxes break the $\mathcal{P}_{X,Y}\mathcal{T}$ symmetry of \mathcal{H}_{SD}^{XY} explicitly, eliminating exceptional points for any or η (Fig. 3b, bottom). The effect of flux is striking for $J \approx \eta$ (Fig. 3c), where we find strong tuning of both frequency and linewidth, with eigenmodes coalescing at the degenerate exceptional points $\Phi \in \{0, 2\pi\}$.

Higher-order exceptional points and chiral amplification

The squeezing dimer behaviour is intrinsically quadrature-dependent, as the paths in quasiparticle space link conjugated elements a_i and a_i^\dagger directly or indirectly. The response to any real excitation (a superposition of a_i 's and a_i^\dagger 's) then depends on the particle–hole phase difference, that is, the excited quadrature. Another example is phase-dependent amplification in the bosonic Kitaev chain (without synthetic flux)^{26,27}. One can, however, conceive loops without such links, expecting quadrature-independent nonreciprocity and chirality (Methods). The Hermitian beamsplitter trimer represents a trivial example, comprising two disjoint loops connecting all particles and holes, respectively (Fig. 4a).

We find a non-Hermitian system encompassing disjoint loops by ‘conjugating’ one resonator in the beamsplitter trimer, that is, swapping $a_3 \leftrightarrow a_3^\dagger$. We implement this ‘singly conjugated trimer’ (SCT) by modulating at $\omega_2 - \omega_1$, $\omega_1 + \omega_3$ and $\omega_2 + \omega_3$. The latter induce two-mode squeezing, specifically $H_{SCT} = e^{i\varphi_{12}} a_2^\dagger a_1 + \eta_{23} e^{i\theta_{23}} a_3 a_2 + \eta_{13} e^{-i\theta_{13}} a_1^\dagger a_3 + \text{H. c.}$, and loops threaded by fluxes $\Phi = \varphi_{12} + \theta_{23} - \theta_{13}$ and $-\Phi$ (Fig. 4a).

The disjoint loop topology of the quasiparticle network implies block-diagonality of the BdG dynamical matrix \mathcal{H}_{SCT} , with non-Hermitian blocks governing the dynamics of each loop. The interplay of Aharonov–Bohm interference and non-Hermiticity in the singly conjugated trimer induces dynamical stability transitions, unmatched by the beamsplitter trimer. Figure 4b shows these as surfaces in J/η - Φ space for $\eta_{13} = \eta_{32} = \eta$ and equal dissipation $\gamma_i = 0$. We identify a stable phase with real eigenfrequencies and an unstable phase with three distinct imaginary parts.

Interestingly, for $J = 2\sqrt{2}\eta$ the (real) eigenvalues of a single loop of \mathcal{H}_{SCT} coincide with those of a homogeneous beamsplitter trimer ($J_{ij} = J$) for all Φ . The thermal spectra in Fig. 4c show, however, that the response around ω_3 associated with the ‘conjugated’ resonator 3 appears frequency-reflected, because particles (holes) evolve with positive (negative) frequencies in the non-rotating frame. Moreover, we observe asymmetries between resonators 1 and 2 in the middle band’s thermal amplitude at $\Phi \in \{\pi/2, 3\pi/2\}$. These asymmetric, flux-controlled localization of fluctuations—unattainable in the beamsplitter trimer if $J_{31} = J_{23}$ —arise from the combination of chirality and squeezing and persist even for vacuum fluctuations (Supplementary Information section IIF). These asymmetries, akin to chiral, incoherently pumped dynamics in \mathcal{PT} -symmetric trimers³⁶, suggest that the singly conjugated trimer functions like a phononic nonreciprocal amplifier^{11,17,18,20}.

We see that the singly conjugated trimer features an exceptional contour in the J/η - Φ parameter space (Fig. 4b), linked to the spontaneous breaking of parity–time ($\mathcal{P}_{gl}\mathcal{T}$) symmetry. Here, the effective mirror symmetry, \mathcal{P}_{gl} , exchanges ‘gainy’ and ‘lossy’ eigenmodes a_{gl} for $J = 0$, namely $a_{gl} = (a_+ \mp ia_3)/\sqrt{2}$ with $\varepsilon_{gl} = \pm\sqrt{2}\eta$ where $a_+ = (a_1 + a_2)/\sqrt{2}$ (gauge $\theta_g = 0$). When $\Phi \in \{0, \pi\}$, a beamsplitter interaction $J > 0$ couples $a_g \leftrightarrow a_i$, constructing a $\mathcal{P}_{gl}\mathcal{T}$ -symmetric dimer with a second-order exceptional point at $J = 2\sqrt{2}\eta$ (Fig. 4d, top). However, for $\Phi \in \{\pi/2, 3\pi/2\}$, a third, neutral mode $a_- = (a_1 - a_2)/\sqrt{2}$ —uncoupled when $\Phi \in \{0, \pi\}$ —couples to a_{lg} in a loss–neutral–gain chain configuration. Interestingly, this trimer features spontaneous $\mathcal{P}_{gl}\mathcal{T}$ -symmetry breaking at a third-order exceptional point at $J = \sqrt{2}\eta$ (Fig. 4d, bottom). Indeed, the presence of a higher-order exceptional point sitting at the nexus of two second-order exceptional contours³⁷ is mandated by eigensurface topology (Fig. 4b).

The flux-induced breaking of \mathcal{P}_{12} (mirror) symmetry impacts specifically the $\mathcal{P}_{gl}\mathcal{T}$ -symmetry-broken phase. In a three-site, gain–neutral–loss chain, \mathcal{PT} -symmetry-broken states delocalize non-uniformly over central and boundary sites (here the pairs a_g/a_- and a_+/a_i)³⁸. Crossing the third-order exceptional point at $\Phi = \pm\pi/2$ biases gain towards the bare oscillator a_1 ($\Phi = \pi/2$) or a_2 ($\Phi = -\pi/2$) as a result. This flux-tunable chiral gain becomes striking in the transient, unstable dynamics of the singly conjugated trimer, as shown in Fig. 4e for gain

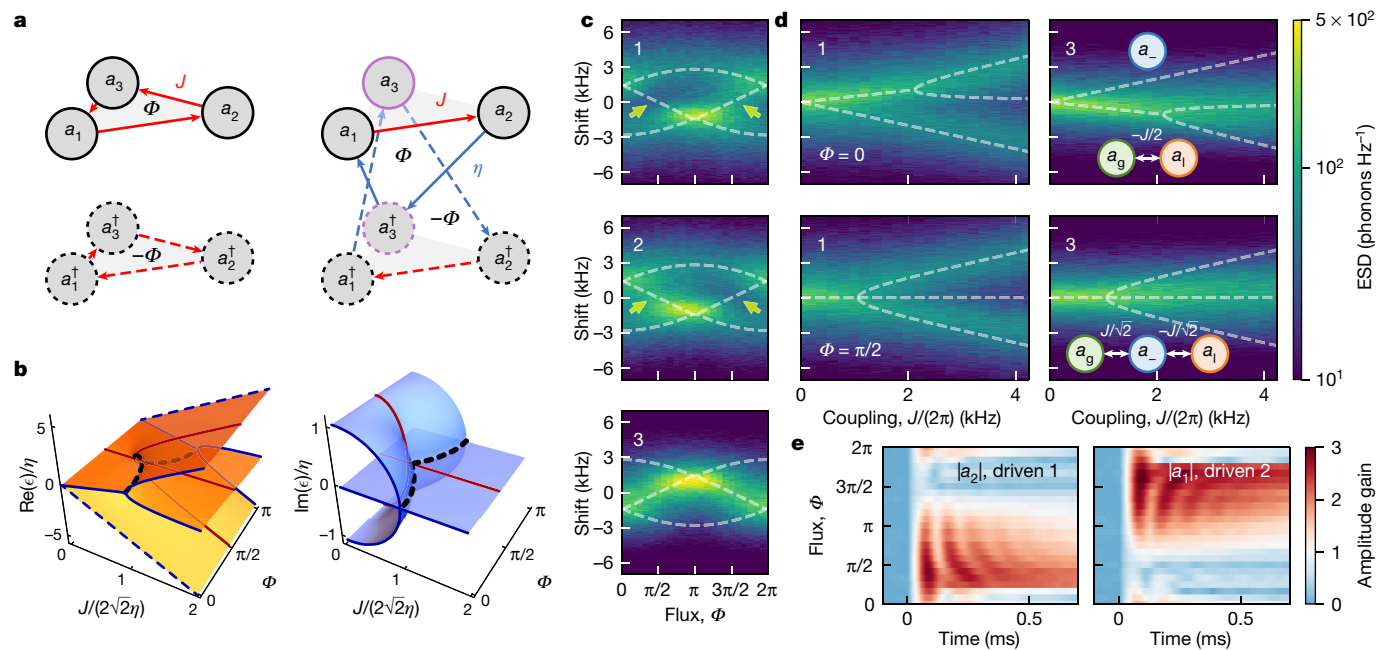


Fig. 4 | Chirality in a non-Hermitian network. **a**, Sketch of the networks in particle–hole space corresponding to the beamsplitter trimer (left) and the singly conjugated trimer (right), manifesting their topological resemblance. **b**, Complex eigensurfaces for the singly conjugated trimer ($\gamma_i = \gamma$) depicted from $\Phi = 0$ to $\Phi = \pi$ for clarity. Imaginary parts are referenced to γ . A black dotted line highlights an exceptional contour separating stable and unstable dynamical phases. **c**, Thermomechanical spectra of the three resonators (top, middle and bottom showing 1–3, respectively) for $\eta/(2\pi) = 1$ kHz, $J = 2\sqrt{2}\eta$. Feedback is used to equalize mechanical loss rates $\gamma_i/(2\pi) = \gamma/(2\pi) = 4$ kHz. The sideband of the ‘conjugated’ resonator 3 is reflected in frequency compared to the other two. Localization of fluctuations is observed, including 1–2 asymmetry indicated by arrows. Theoretical eigenfrequencies are shown as

dashed lines. **d**, Spectra for resonators 1 (left) and 3 (right) for $\eta/(2\pi) = 0.75$ kHz for a trivial flux $\Phi = 0$ (top), and in the maximally chiral case $\Phi = \pi/2$ (bottom). The flux-dependent coupling topology for the effective resonators g , l and morphs a second-order exceptional point into a third-order one (see text). Insets show the effective \mathcal{PT} -symmetric dimer/trimer structure for both flux values. **e**, The ratio between instantaneous and initial coherent amplitudes (normalized to phonon number), in the unstable and nonlinear regime $\eta/(2\pi) = \gamma/(2\pi) = 5$ kHz, without feedback (mechanical loss rates $\gamma_i/(2\pi) = \{2.5, 1.6, 4.1\}$ kHz). Resonator 1 (left) or 2 (right) is driven for $t < 0$, and couplings are established when $t > 0$. This induces chirally amplified transport to the other resonator and (decohering) self-oscillation bounded by nonlinear dynamics.

exceeding dissipation. There, an initial excitation in resonator 1 (2) is amplified coherently—above initial amplitudes—towards 2 (1) for flux $\Phi = \pi/2$ ($\Phi = \pi/2$), and attenuated quickly in the opposite direction. Conversely, for $\Phi = 0$, gain distributed evenly over resonators 1 and 2 leads to reciprocal dynamics. Linear analysis breaks down as the system crosses the instability threshold ($\text{Im}(\epsilon) > 0$), where we see optomechanically induced Duffing nonlinearities cause amplitude saturation and self-oscillations, even at only a few times the thermal amplitude. Indeed, this points the way to investigating strongly nonlinear systems with broken Hermiticity and time-reversal symmetry.

In conclusion, we observed chiral, non-Hermitian phonon dynamics in nano-optomechanical networks with fully controlled beamsplitter and squeezing interactions. New geometrical phases act on excitations in particle–hole space that control \mathcal{PT} symmetry through a non-Hermitian Aharonov–Bohm effect. The resulting phenomena of tunable squeezing, (higher-order) exceptional points and nonreciprocal amplification point to applications in nanomechanical sensing³⁹, signal processing⁴¹ and Ising machines⁴⁰. These mechanisms will be equally powerful in other bosonic domains, from photonics to cold atoms. Although the effects were probed with thermal and coherent excitations, they persist down to the quantum domain, forming essential ingredients to explore new linear and nonlinear non-Hermitian topological phases.

Online content

Any methods, additional references, Nature Research reporting summaries, source data, extended data, supplementary information, acknowledgements, peer review information; details of author

contributions and competing interests; and statements of data and code availability are available at <https://doi.org/10.1038/s41586-022-04609-0>.

- Cohen, E. et al. Geometric phase from Aharonov–Bohm to Pancharatnam–Berry and beyond. *Nat. Rev. Phys.* **1**, 437–449 (2019).
- Bergholtz, E. J., Budich, J. C. & Kunst, F. K. Exceptional topology of non-Hermitian systems. *Rev. Mod. Phys.* **93**, 015005 (2021).
- Coulais, C., Fleury, R. & van Wezel, J. Topology and broken Hermiticity. *Nat. Phys.* **17**, 9–13 (2021).
- Lieu, S. Topological symmetry classes for non-Hermitian models and connections to the bosonic Bogoliubov–de Gennes equation. *Phys. Rev. B* **98**, 115135 (2018).
- Gong, Z. et al. Topological phases of non-Hermitian systems. *Phys. Rev. X* **8**, 031079 (2018).
- St-Jean, P. et al. Lasing in topological edge states of a one-dimensional lattice. *Nat. Photonics* **11**, 651–656 (2017).
- Hu, B. et al. Non-Hermitian topological whispering gallery. *Nature* **597**, 655–659 (2021).
- Zeuner, J. M. et al. Observation of a topological transition in the bulk of a non-Hermitian system. *Phys. Rev. Lett.* **115**, 040402 (2015).
- Barnett, R. Edge-state instabilities of bosons in a topological band. *Phys. Rev. A* **88**, 063631 (2013).
- Peano, V., Houde, M., Brendel, C., Marquardt, F. & Clerk, A. A. Topological phase transitions and chiral inelastic transport induced by the squeezing of light. *Nat. Commun.* **7**, 10779 (2016).
- Peano, V., Houde, M., Marquardt, F. & Clerk, A. A. Topological quantum fluctuations and traveling wave amplifiers. *Phys. Rev. X* **6**, 041026 (2016).
- Bandres, M. A. et al. Topological insulator laser: experiments. *Science* **359**, eaar4005 (2018).
- Ghatak, A., Brandenbourger, M., van Wezel, J. & Coulais, C. Observation of non-Hermitian topology and its bulk-edge correspondence in an active mechanical metamaterial. *Proc. Natl Acad. Sci. USA* **117**, 29561–29568 (2020).
- Helbig, T. et al. Generalized bulk-boundary correspondence in non-Hermitian topoelectrical circuits. *Nat. Phys.* **16**, 747–750 (2020).
- Weidemann, S. et al. Topological funneling of light. *Science* **368**, 311–314 (2020).

16. Wang, K. et al. Generating arbitrary topological windings of a non-Hermitian band. *Science* **371**, 1240–1245 (2021).
17. Sliwa, K. M. et al. Reconfigurable Josephson circulator/directional amplifier. *Phys. Rev. X* **5**, 041020 (2015).
18. Ruesink, F., Miri, M.-A., Alù, A. & Verhagen, E. Nonreciprocity and magnetic-free isolation based on optomechanical interactions. *Nat. Commun.* **7**, 13662 (2016).
19. Fang, K. et al. Generalized non-reciprocity in an optomechanical circuit via synthetic magnetism and reservoir engineering. *Nat. Phys.* **13**, 465–471 (2017).
20. Mercier de Lépinay, L., Ockeloen-Korppi, C. F., Malz, D. & Sillanpää, M. A. Nonreciprocal transport based on cavity Floquet modes in optomechanics. *Phys. Rev. Lett.* **125**, 023603 (2020).
21. Huber, S. D. Topological mechanics. *Nat. Phys.* **12**, 621–623 (2016).
22. Ozawa, T. et al. Topological photonics. *Rev. Mod. Phys.* **91**, 015006 (2019).
23. Miri, M.-A. & Alù, A. Exceptional points in optics and photonics. *Science* **363**, eaar7709 (2019).
24. Özdemir, S. K., Rotter, S., Nori, F. & Yang, L. Parity-time symmetry and exceptional points in photonics. *Nat. Mater.* **18**, 783–798 (2019).
25. Wang, Y. X. & Clerk, A. A. Non-Hermitian dynamics without dissipation in quantum systems. *Phys. Rev. A* **99**, 063834 (2019).
26. Flynn, V. P., Cobanera, E. & Viola, L. Deconstructing effective non-Hermitian dynamics in quadratic bosonic Hamiltonians. *New J. Phys.* **22**, 083004 (2020).
27. McDonald, A., Pereg-Barnea, T. & Clerk, A. A. Phase-dependent chiral transport and effective non-Hermitian dynamics in a bosonic Kitaev–Majorana chain. *Phys. Rev. X* **8**, 041031 (2018).
28. Wanjura, C. C., Brunelli, M. & Nunnenkamp, A. Topological framework for directional amplification in driven-dissipative cavity arrays. *Nat. Commun.* **11**, 3149 (2020).
29. Aspelmeyer, M., Kippenberg, T. J. & Marquardt, F. Cavity optomechanics. *Rev. Mod. Phys.* **86**, 1391–1452 (2014).
30. Xu, H., Jiang, L., Clerk, A. A. & Harris, J. G. E. Nonreciprocal control and cooling of phonon modes in an optomechanical system. *Nature* **568**, 65–69 (2019).
31. Mathew, J. P., del Pino, J. & Verhagen, E. Synthetic gauge fields for phonon transport in a nano-optomechanical system. *Nat. Nanotechnol.* **15**, 198–202 (2020).
32. Koutserimpas, T. T. & Fleury, R. Non-reciprocal gain in non-Hermitian time-Floquet systems. *Phys. Rev. Lett.* **120**, 087401 (2017).
33. Roushan, P. et al. Chiral ground-state currents of interacting photons in a synthetic magnetic field. *Nat. Phys.* **13**, 146–151 (2017).
34. Habraken, S. J., Stannigel, K., Lukin, M. D., Zoller, P. & Rabl, P. Continuous mode cooling and phonon routers for photonic quantum networks. *New J. Phys.* **14**, 115004 (2012).
35. Huber, J. S. et al. Spectral evidence of squeezing of a weakly damped driven nanomechanical mode. *Phys. Rev. X* **10**, 021066 (2020).
36. Downing, C. A., Zueco, D. & Martín-Moreno, L. Chiral current circulation and \mathcal{PT} symmetry in a trimer of oscillators. *ACS Photonics* **7**, 3401–3414 (2020).
37. Tang, W. et al. Exceptional nexus with a hybrid topological invariant. *Science* **370**, 1077–1080 (2020).
38. Hodaei, H. et al. Enhanced sensitivity at higher-order exceptional points. *Nature* **548**, 187–191 (2017).
39. Lau, H.-K. & Clerk, A. A. Fundamental limits and non-reciprocal approaches in non-Hermitian quantum sensing. *Nat. Commun.* **9**, 4320 (2018).
40. Mahboob, I., Okamoto, H. & Yamaguchi, H. An electromechanical Ising Hamiltonian. *Sci. Adv.* **2**, e1600236 (2016).

Publisher's note Springer Nature remains neutral with regard to jurisdictional claims in published maps and institutional affiliations.

Springer Nature or its licensor (e.g. a society or other partner) holds exclusive rights to this article under a publishing agreement with the author(s) or other rightsholder(s); author self-archiving of the accepted manuscript version of this article is solely governed by the terms of such publishing agreement and applicable law.

© The Author(s), under exclusive licence to Springer Nature Limited 2022, corrected publication 2022

Article

Methods

Effective mechanical Hamiltonian

We present a comprehensive theoretical model for the optomechanically mediated nanomechanical interactions in our platform. A cavity mode with frequency ω_c and photon loss rate κ is coupled to an ensemble of mechanical modes with frequencies ω_i (index $i \in \{1, 2, \dots, N\}$) with vacuum optomechanical coupling rates $g_0^{(i)}$, according to the Hamiltonian

$$\tilde{H}_s = \sum_i \omega_i \tilde{a}_i^\dagger \tilde{a}_i - \Delta c^\dagger c - \sum_i g_0^{(i)} c^\dagger c (\tilde{a}_i + \tilde{a}_i^\dagger). \quad (3)$$

Here, mechanical annihilation operators in the lab frame are denoted by \tilde{a}_i and we set $\hbar = 1$. Operators \tilde{a}_i correspond to distinct mechanical eigenmodes ('resonators'), which form a 'synthetic dimension' along which we study mode hybridization and excitation transport^{41,42}. The cavity field annihilation operator c is expressed in the rotating frame of a control laser field at frequency ω_L detuned by $\Delta = \omega_L - \omega_c$ from the cavity resonance. We operate in the regime of large detuning and bandwidth ($\Delta, \kappa \gg \omega_i$). With cavity in-coupling rate κ_{in} , a control field with slowly varying amplitude $c_{in}(t)$ addresses the intracavity photon population instantaneously, displacing the cavity mode by a steady-state amplitude approximated by the $g_0^{(i)} = 0$ solution,

$$\bar{c}(t) \approx \sqrt{\kappa_{in}} \chi_c c_{in}(t), \quad (4)$$

with bare cavity susceptibility $\chi_c = \left(\frac{\kappa}{2} - i\Delta\right)^{-1}$. Typical values for κ_{in} and average optical power $\langle P \rangle_t = \hbar \omega_L \langle |c_{in}(t)|^2 \rangle_t$ lie in the range of $\kappa_{in} \approx 0.03\kappa$ and $\langle P \rangle_t = 1.0$ mW, respectively.

We linearize the radiation-pressure interaction equation (3) by displacing the cavity amplitude around equation (4), that is, $c(t) \rightarrow \bar{c}(t) + \delta c(t)$ and neglecting terms $\mathcal{O}((\delta c)^2)$, assuming small cavity fluctuations $\delta c(t)$. In a subsequent step, we find an effective phononic Hamiltonian by carrying out a second-order perturbation treatment to the linearized interaction, consisting of adiabatic elimination of the fluctuations δc through the approach in ref. ⁴³. This approximation is valid provided that cavity fluctuations reach a steady state of low amplitude at the fastest timescale of the system, as prescribed by $\kappa, \Delta \gg \omega_i$. The detailed procedure can be found in Supplementary Information section IA. In rotating frames at ω_i , accessed via unitary transformation $U_F = \exp(-i\sum_i \omega_i \tilde{a}_i^\dagger \tilde{a}_i)$, mechanical operators read $a_i = U_F \tilde{a}_i U_F^\dagger = e^{i\omega_i t} \tilde{a}_i$. Moreover, the effective phononic Hamiltonian $U_F \tilde{H}_{\text{eff}} U_F^\dagger = H_{\text{eff}} = H_g + H_{\text{eff}}^{\text{int}}$ decomposes into a displacement term $H_g = -|\bar{c}(t)|^2 [\sum_i g_0^{(i)} (a_i e^{-i\omega_i t} + \text{H.c.})]$ and the interaction Hamiltonian,

$$H_{\text{eff}}^{\text{int}} \approx \Delta \kappa_{in} |\chi_c|^4 c_{in}(t)^2 \left[\sum_i g_0^{(i)} (a_i e^{-i\omega_i t} + \text{H.c.}) \right]^2. \quad (5)$$

We introduce modulation of the control field intensity $|c_{in}(t)|^2$ using multiple harmonic driving tones l with frequencies $\omega_m^{(l)}$, modulation depths $c_m^{(l)}$ and phases $\phi_m^{(l)}$. The homogeneous intracavity intensity responds linearly as (equation (4)) $n_c(t) \approx |\bar{c}(t)|^2 = \bar{n}_c [1 + \sum_l c_m^{(l)} \cos(\omega_m^{(l)} t + \phi_m^{(l)})]$, where $\bar{n}_c = \kappa_{in} |\chi_c|^2 |\bar{c}_{in}|^2$ is the average photon number.

In the next step, we apply the rotating wave approximation, which retains only the co-rotating terms with slow evolution in the rotating frame. The rotating wave approximation assumes moderate couplings compared with natural oscillation frequencies and narrow mechanical linewidth $\gamma_l \ll \omega_i$. Considering that dynamical modulations are not resonant with any vibrational mode ($\omega_m^{(l)} \neq \omega_i$), the relevant contributions in equation (5) thus read $H_{\text{eff}}^{\text{int}} \approx \sum_{i,j} H_{ij}^{(i,j)}$ with $i, j \in \{1, 2, \dots, N\}$,

$$H_{\text{eff}}^{(i,j)} = g(t) (a_i e^{-i\omega_i t} + \text{H.c.}) (a_j e^{-i\omega_j t} + \text{H.c.}), \quad (6)$$

and $g(t) = \Delta |\chi_c|^2 g_0^{(i)} g_0^{(j)} n_c(t)$. The static component of $n_c(t)$ is responsible for an optical shift of the mechanical spring constant by $\omega_i \mapsto \omega_i + \delta\omega_i$

that is reabsorbed in the definition of ω_i , where $\delta\omega_i = 2g_i^2\Delta/(\Delta^2 + \kappa^2/4)$ and $g_i = g_0^{(i)} \sqrt{\bar{n}_c}$ denotes the cavity-enhanced optomechanical coupling rate²⁹. Crucially, the time-dependent part in equation (6) corresponds to mechanical interactions that can be selected by suitably resonant modulation tones l , while imprinting $\phi_m^{(l)}$ as a Peierls phase on the interaction^{31,44}. Within a subsequent rotating wave approximation, the remaining interaction terms in equation (6) correspond to the modulation frequencies $\omega_m^{(l)}$ either approaching (i) a frequency sum $\Sigma\omega^{(ij)} = \omega_i + \omega_j$, or (ii) a frequency difference $\Delta\omega^{(ij)} = \omega_i - \omega_j$, with $i, j \in \{1, 2, \dots, N\}$. The rotating wave approximation is valid for moderate effective coupling strengths $J_{ij}, \eta_{ij} \ll \omega_i$ (defined below; in the experiment, $J_{ij}/\omega_i, \eta_{ij}/\omega_i \approx 10^{-3}\text{--}10^{-2}$), resolved-mechanical sidebands (in the experiment, $\gamma_l/\omega_i \approx 10^{-3}\text{--}10^{-2}$) and moderate detuning of the control tones, as well as no commensurable frequency scales ($\omega_i \pm \omega_j \neq \omega_k$ for all modes i, j, k). Equation (3) finally approximates to

$$H_{\text{eff}} \approx \sum_{\omega_m^{(l)} = \Delta\omega^{(ij)}} J_{ij} a_i^\dagger a_j e^{-i[(\omega_m^{(l)} - \Delta\omega^{(ij)})t + \phi_{ij}]} + \text{H.c.} \\ + \sum_{\omega_m^{(l)} = \Sigma\omega^{(ij)}} \eta_{ij} a_i^\dagger a_j e^{-i[(\omega_m^{(l)} - \Sigma\omega^{(ij)})t + \theta_{ij}]/2} + \text{H.c.}, \quad (7)$$

where the sums run over the tones l and indices $\langle i, j \rangle$ that satisfy the specified resonance condition. Note that a single pair of indices $\langle i, j \rangle$ satisfies resonance with a difference frequency $\Delta\omega^{(ij)}$, whereas resonance with a sum frequency $\Sigma\omega^{(ij)}$ is satisfied by both $\langle i, j \rangle$ and $\langle j, i \rangle$.

The hopping (squeezing) amplitudes, denoted J_{ij}, η_{ij} , are proportional to the modulation depth $c_m^{(l)}$ of the corresponding drive tone l ^{31,45} and read:

$$\{J_{ij}, \eta_{ij}\} = c_m^{(l)} \frac{g_i g_j \Delta}{(\Delta^2 + \kappa^2/4)} = c_m^{(l)} \frac{\sqrt{\delta\omega_i \delta\omega_j}}{2}. \quad (8)$$

In the fast-cavity limit photon losses thus simply renormalize the coupling amplitudes J_{ij}, η_{ij} . Similarly, the hopping (squeezing) phases, denoted $\phi_{ij}(\theta_{ij})$, are equal to the corresponding modulation phase $\phi_m^{(l)}$.

Besides moderate effective coupling, the rotating wave approximation relies on the assumption that the modulated drive is quasi-resonant with each relevant process. In the large detuning and parametric drive limit, considerable deviations are expected⁴⁶. Parametric resonators are more naturally treated in this case in terms of the natural amplitudes x (refs. ^{47,48}) or employing quadratures in a generalized rotating frame⁴⁹. For modulation frequencies resonant with $\Delta\omega^{(ij)}, \Sigma\omega^{(ij)}$, equation (7) is exactly time-independent. In this limit, we encode the beamsplitter interactions that conserve the phonon number $n_{ph} = \sum_{i=1}^N a_i^\dagger a_i$ in the elements $A_{ij} = J_{ij} e^{-i\phi_{ij}}, A_{ji} = A_{ij}^*$ of the Hermitian 'hopping matrix' \mathcal{A} . Subsequently, we define the symmetric 'squeezing matrix' \mathcal{B} that encodes the particle-non-conserving squeezing interactions in its elements $B_{ij} = \eta_{ij} e^{i\theta_{ij}}, B_{ji} = B_{ij}^*$. Equation (7) then writes succinctly as the general quadratic form

$$H_{\text{eff}} \approx \sum_{i,j} a_i^\dagger \mathcal{A}_{ij} a_j + \frac{1}{2} (a_i^\dagger \mathcal{B}_{ij} a_j^\dagger + a_i \mathcal{B}_{ij}^* a_j). \quad (9)$$

The matrices \mathcal{A} and \mathcal{B} are provided for the example systems studied in the text explicitly in Supplementary Information section IC.

Bogoliubov–de Gennes framework and symmetries

The effective (time-independent) Hamiltonian in the rotating frame equation (9) allows for a straightforward application of the toolbox of quadratic bosonic Hamiltonians. After defining the Nambu-like vector $\alpha = (\mathbf{a}, \mathbf{a}^\dagger)^T$, with $\mathbf{a} = (a_1, \dots, a_N)$ and where T indicates the transpose, equation (9) is rewritten as (up to a constant offset)

$$H_{\text{eff}} = \frac{1}{2} \alpha^\dagger H \alpha, \quad H = \begin{pmatrix} \mathcal{A} & \mathcal{B} \\ \mathcal{B}^* & \mathcal{A}^* \end{pmatrix}. \quad (10)$$

To faithfully model the ubiquitous mechanical dissipation and thermal fluctuations in the experiment, we introduce coupling to N independent environmental baths in a Heisenberg–Langevin formalism⁵⁰. The corresponding equation of motion for mechanical modes, namely $\dot{\alpha}(t) = -i\mathcal{M}\alpha(t) + \alpha_{in}(t)$ depends on the open-system dynamical matrix $\mathcal{M} = \mathcal{H} - i\Gamma/2$, containing the dissipation matrix $\Gamma = \text{diag}(\gamma_1, \dots, \gamma_N, \gamma_1, \dots, \gamma_N)$, and the BdG dynamical matrix^{51,52}

$$\mathcal{H} = \Sigma_z H = \begin{pmatrix} \mathcal{A} & \mathcal{B} \\ -\mathcal{B}^* & -\mathcal{A}^* \end{pmatrix}, \quad (11)$$

where $\Sigma_z = \text{diag}(1, -1) = [\alpha, \alpha^\dagger]$ encodes bosonic commutation relations. Note that treating creation and annihilation operators, a_i and a_i^\dagger , as separate entities in H and \mathcal{H} shows closed dynamics in particle–hole space. Cavity-mediated corrections to mechanical dissipation ($\gamma_K/(\Delta^2 + \kappa^2) \ll 1$)²⁹ will be neglected. The rotating (scaled) source terms $\alpha_{in} = (\alpha_{in}, \alpha_{in}^\dagger)^\top$ represent baths with Bose occupations $\bar{n}_i \approx k_B T/\omega_i$. These fulfil the same Markovian correlations as their lab-frame counterparts, that is, $\langle \alpha_{in}(t)\alpha_{in}^\dagger(t') \rangle = \mathcal{D}\delta(t-t')$ with diffusion matrix $\mathcal{D} = \text{diag}(\gamma_1(\bar{n}_1+1), \dots, \gamma_1\bar{n}_1, \dots)^{53}$.

When squeezing interactions—which inter-convert particles and holes—are absent ($\mathcal{B} = 0$), the dynamics of a_i and a_i^\dagger are independent, and simply governed by the Hermitian matrices \mathcal{A} and $-\mathcal{A}^*$, respectively. On top of this, if $\Gamma = \gamma \mathbb{1}$, where $\mathbb{1}$ is the identity matrix, the dynamics can be simply mapped to the closed system via a rigid displacement of the imaginary parts of eigenvalues by $\gamma/2$. This displacement is equivalent to a dynamically offset basis transformation $\alpha'(t) = \exp\left(\frac{\gamma}{2}t\right)\alpha(t)$, relating solutions of ideal and dissipative harmonic oscillators⁵⁴. Therefore, whenever $\mathcal{B} = 0$ is zero, we say that the mechanical modes undergo Hermitian dynamics. However, even for $\Gamma = 0$, \mathcal{M} and \mathcal{H} are non-Hermitian if squeezing is present ($\mathcal{B} \neq 0$). We state mechanical modes thus manifest non-Hermitian dynamics in that case.

The time evolution of the mechanical amplitudes $\alpha'(t)$ can be expressed in terms of the spectral decomposition of \mathcal{H} (Supplementary Information section IC). A non-Hermitian \mathcal{H} can host eigenvectors with complex eigenfrequencies ϵ . The different character of eigenfrequencies or ‘dynamical phases’ in parameter space links to generalized parity–time (GPT) symmetries of \mathcal{H} and the associated eigenvectors fulfilling or spontaneously breaking the symmetry²⁶. For example, purely oscillatory eigenmodes (real eigenfrequencies) indicate a stable phase (eigenvectors fulfil GPT symmetry), whereas positive imaginary eigenfrequencies indicate an unstable phase (eigenvectors break GPT symmetry). We note that GPT symmetry coexists with other built-in symmetries of \mathcal{H} that reflect $a_i - a_i^\dagger$ splitting redundancies and must be always fulfilled by eigenvectors (Supplementary Information section IC).

For homogeneous dissipation ($\gamma_i = \gamma$), the symmetries of the open-system dynamical matrix \mathcal{M} are trivially related to those of \mathcal{H} , because $\mathcal{M} \mapsto \mathcal{H}$ in the dynamically offset basis $\alpha'(t)$. The symmetry classification of \mathcal{H} thus offers insight on dynamical phases, eigensurface topology and symmetry breaking in the open system. As an example, PT symmetry in \mathcal{H} ^{55,56} corresponds to ‘quasi’ or ‘passive’ PT symmetry in \mathcal{M} ^{24,57,58}. Similar dynamical mode offsets are also of service in the generalization to non-symmetric cases (Supplementary Information section IIC).

In our systems, a dynamical phase transition (that is, spontaneous symmetry breaking) is often accompanied by an exceptional point^{38,59}, where eigenvalues and eigenvectors simultaneously coalesce and \mathcal{H} is non-diagonalizable. Alternatively, eigenvalues can split off the real axis without diagonalizability loss²⁶. Coalescences are analysed in the studied systems by analytical diagonalization (see Supplementary Information section IIB–E). Defective eigenvector subspaces of \mathcal{H} can also be detected by large numerical values of the condition number for the inverse of the eigenvector matrix⁶⁰.

Graph representation of quadratic bosonic Hamiltonians and quadrature-independent transport

The existence of a nontrivial gauge field is equivalent to the breaking of time-reversal symmetry (that is, under the operation \mathcal{T}), which signifies that the Hamiltonian matrix H cannot be rendered real ($H \neq H^*$) via $U(1)$ gauge transformations. This statement is equivalent to having a gauge-invariant synthetic flux in the system⁶¹. We introduce a powerful graphical representation for the Hamiltonian in equation (10), revealing loops and nontrivial $U(1)$ synthetic fluxes in particle–hole (Bogoliubov) space. Our graphical framework avoids self-loops in the dynamical matrix representation, previously introduced to describe on-site parametric gain⁶². We consider \mathcal{A} and \mathcal{A}^* as the adjacency matrices for network graphs \mathcal{G}_a and \mathcal{G}_{a^\dagger} , disposed in two layers, where nodes correspond to a_i and a_i^\dagger operators, respectively (Extended Data Fig. 3).

In this representation, particle-conserving systems ($\mathcal{B} = 0$, Hermitian equation (11)) feature disjoint network layers, whereas parametric gain ($\mathcal{B} \neq 0$, non-Hermitian equation (11)) introduces links between \mathcal{G}_a and \mathcal{G}_{a^\dagger} through \mathcal{B} and back via \mathcal{B}^* . We note that graph representations for the Hamiltonian and the BdG matrices are similar, as they allow recognizing loops in particle–hole space with geometrical phases differing by π . Namely, \mathcal{H} graphs contain layers with adjacency matrices \mathcal{A} and $-\mathcal{A}^*$, connected with each other through \mathcal{B} and $-\mathcal{B}^*$.

This graph representation gives insight into general features of energy transport. In particular, quadrature-independent excitation dynamics is found in networks that feature disjoint graphs (for example, loops), which do not contain direct or indirect links between particles a_i and their corresponding holes a_i^\dagger (Fig. 4). This sublattice symmetry implies pairs of uncoupled blocks in \mathcal{H} , which govern the nodes $\alpha_L = (a_i, \dots, a_j^\dagger)$ and $\alpha_{L^*}^\dagger$ in (independent) graphs L, L^* . For M disjoint graph pairs, the permutation of the modes α into each of the graphs, $\alpha \mapsto \Pi\alpha = (\alpha_{L_1}, \alpha_{L_1}^\dagger, \dots, \alpha_{L_M}, \alpha_{L_M}^\dagger)^\top$, block-diagonalizes \mathcal{H} :

$$\mathcal{H} \mapsto \mathcal{H}' = \Pi\mathcal{H}\Pi = \text{diag}(\mathcal{L}_1, -\mathcal{L}_1^*, \dots, \mathcal{L}_M, -\mathcal{L}_M^*). \quad (12)$$

Owing to charge-conjugation symmetry \mathcal{C} , particle–hole loops come in pairs. If such loops are disjoint, their associated dynamical matrices $\mathcal{L}_m - \mathcal{L}_m^*$ ($m = 1, \dots, M$), will never mix particles and their corresponding hole excitations as they propagate through the graphs. In a single loop pair (Fig. 4), dropping the index m ,

$$\mathbf{n}(t) = e^{i\mathcal{L}^*t} \mathbf{n}(0) e^{-i\mathcal{L}t}, \quad n_i = a_i^\dagger a_i, \quad (13)$$

having formally integrated $i\dot{\alpha}_L = \mathcal{L}\alpha_L$ and $i\dot{\alpha}_L^\dagger = -\mathcal{L}^*\alpha_L^\dagger$ that is, employing conjugated blocks. Population dynamics in equation (13) are independent of the relative phases between $a_i(0)$ and $a_i^\dagger(0)$, that is, the resonator i quadrature.

Non-Hermitian Aharonov–Bohm effect

The squeezing dimer shown in Fig. 2 presents the minimal instance of a plaquette in particle–hole space permeated by a nontrivial flux, and illustrates the contrast between the Hermitian and non-Hermitian Aharonov–Bohm effects. Here we describe how the latter is manifested in the flux-dependent coupling of gain/lossy quadratures, whereas we focus on effects in the complex ‘energy’ eigenbasis in Supplementary Information sections ID, IIB.

The combination of particle–hole conversions with a geometrical Aharonov–Bohm phase along two superimposed loops L and L^* leads to a redistribution of gain and squeezing in the dimer hybrid quadratures. We choose the gauge $\theta_i = \pi/2$, for which the local resonator quadratures $X_i = (a_i + a_i^\dagger)/\sqrt{2}$ ($Y_i = i(a_i^\dagger - a_i)/\sqrt{2}$) experience loss (gain) in the beamsplitter-uncoupled limit ($J = 0$). The flux in this gauge reads $\Phi = 2\varphi_{12}$. Quadrature interactions can be decomposed in terms of

Article

particle-hole conversions along the two loops, that is, $\mathcal{H}_{\text{SD}} = \mathcal{H}_{\text{SD}}^L + \mathcal{H}_{\text{SD}}^{L'}$ (loop order $\{a_1, a_2, a_2^\dagger, a_1^\dagger\}$), with

$$\mathcal{H}_{\text{SD}}^L = \begin{pmatrix} 0 & J & 0 & 0 \\ 0 & 0 & -i\eta & 0 \\ 0 & 0 & 0 & -J \\ -i\eta & 0 & 0 & 0 \end{pmatrix}, \quad \mathcal{H}_{\text{SD}}^{L'} = (\Sigma_z \mathcal{H}_{\text{SD}}^L \Sigma_z)^\dagger, \quad (14)$$

where $J = J \exp\left(-\frac{i\phi}{2}\right)$. $\mathcal{H}_{\text{SD}}^L$ and $\mathcal{H}_{\text{SD}}^{L'}$ reflect clockwise and counter-clockwise propagation of excitations.

The dynamical matrix $\mathcal{H}_{\text{SD}}^{XY} = Q^\dagger \mathcal{H}_{\text{SD}}^L Q + Q^\dagger \mathcal{H}_{\text{SD}}^{L'} Q$ is obtained by applying the mapping to the quadrature basis Q (order $\{X_1, X_2, Y_1, Y_2\}$):

$$\mathcal{H}_{\text{SD}}^{XY} = \begin{pmatrix} -i\eta & -iJ_{||} & 0 & iJ_{\perp} \\ iJ_{||} & -i\eta & iJ_{\perp} & 0 \\ 0 & -iJ_{\perp} & i\eta & -iJ_{||} \\ -iJ_{\perp} & 0 & iJ_{||} & i\eta \end{pmatrix}. \quad (15)$$

The combination of clockwise and counter-clockwise processes with nontrivial Peierls phases then leads to the flux-dependent couplings $J_{||} = J \sin(\phi/2)$ and $J_{\perp} = J \cos(\phi/2)$ between quadratures.

Gain-loss bases and effective PT symmetries

Adequate bases for the squeezing dimer and the singly conjugated trimer can be determined for which one easily recognizes an inversion plane separating gain and loss at either side, and therefore potentially a \mathcal{PT} symmetry. For the squeezing dimer, such symmetry is found using the local quadratures $\mathbf{R}_{\text{SD}} = (X_1, Y_2, X_2, Y_1)^\top$. In a $\theta_i = \pi/2$ gauge, equation (15) is block-diagonal for $\phi = 0$ and reads $\mathcal{H}_{\text{SD}}^{XY} = \text{diag}(\mathcal{H}^{X_1, Y_2}, \mathcal{H}^{X_2, Y_1})$ with the blocks

$$\mathcal{H}^{X_1, Y_2} = i \begin{pmatrix} -\eta & J \\ -J & \eta \end{pmatrix} = \mathcal{H}^{X_2, Y_1}, \quad (16)$$

governing the dynamics of the independent ‘quadrature dimers’ $X_1 Y_2$ and $X_2 Y_1$. Their closed-system equations of motion read $\dot{\mathbf{R}}_{\text{SD}} = -i\mathcal{H}_{\text{SD}}^{XY} \mathbf{R}_{\text{SD}}$.

Each of the blocks equation (16) is $\mathcal{P}_{X_i Y_j} \mathcal{T}$ -symmetric, with parity operation $\mathcal{P}_{X_i Y_j}: X_i \leftrightarrow Y_j$ and effective \mathcal{T} equivalent to complex conjugation: $i \mapsto -i$. The eigenfrequencies for each block equation (16), namely $\varepsilon^{X_i Y_j} = \pm \sqrt{J^2 - \eta^2}$, are real within the $\mathcal{P}_{X_i Y_j} \mathcal{T}$ -symmetric region $J > \eta$, in which the corresponding eigenstates respect the symmetry of the dynamical matrix. This is no longer true if $J \leq \eta$, where $\mathcal{P}_{X_i Y_j} \mathcal{T}$ is spontaneously broken, with a second-order exceptional point at $J = \eta$ indicating the transition.

The recognition of this \mathcal{PT} symmetry enables an explanation of why nonzero fluxes imply complex, non-real eigenvalues and the disappearance of the exceptional point: they induce coupling between the sub-blocks equation (16) and the explicit breaking of $\mathcal{P}_{X_i Y_j} \mathcal{T}$ symmetry. This dynamical phase transition along $\phi \geq 0$ from real to complex eigenvalues can equivalently be characterized in terms of spontaneous \mathcal{GPT} symmetry breaking without loss of diagonalizability²⁶. An extended theoretical analysis shows that asymmetries in the squeezing dimer negligibly shift the location of degeneracies in the experiment, and lead in general to the expansion of exceptional points into contours in parameter space (Supplementary Information section IIC).

Similarly, the dynamical phases of the singly conjugated trimer can be classified by \mathcal{GPT} symmetries. The maximum degree of symmetry and degeneracy order corresponds to equal dissipation rates ($\gamma_i = \gamma$). In experiment, we match dissipation rates by applying feedback control. The dynamics of the singly conjugated trimer can be integrated, recognizing dynamical phase transitions, via a single block of \mathcal{H}' (equation (12)): the block acting on $\{a_1, a_2, a_3^\dagger\}$ (gauge $\theta_{23} = \theta_{13} = 0$, where the flux simply reads $\phi = \varphi_{12}$),

$$\mathcal{L} = \begin{pmatrix} 0 & Je^{-i\phi} & \eta \\ Je^{i\phi} & 0 & \eta \\ -\eta & -\eta & 0 \end{pmatrix}. \quad (17)$$

A \mathcal{GPT} symmetry is straightforwardly recognized by switching to the eigenbasis of equation (17) for vanishing beamsplitter coupling ($J = 0$), via the unitary transformation

$$U_{\text{gl}} = \frac{1}{\sqrt{2}} \begin{pmatrix} \frac{i}{\sqrt{2}} & -\frac{i}{\sqrt{2}} & -1 \\ \frac{i}{\sqrt{2}} & -\frac{i}{\sqrt{2}} & 1 \\ 1 & 1 & 0 \end{pmatrix}. \quad (18)$$

The corresponding eigenmodes $U_{\text{gl}} \alpha$ are denoted as $a_l = (a_3^\dagger + ia_2)/\sqrt{2}$ (where $a_+ = (a_1 + a_2)/\sqrt{2}$ is the symmetric superposition of resonator 1 and 2 states), $a_g = (a_3^\dagger - ia_2)/\sqrt{2}$ and $a_- = (a_1 - a_2)/\sqrt{2}$. Adopting the order $\{a_l, a_g, a_-\}$, the transformed matrix $\mathcal{L}_{\text{gl}} = U_{\text{gl}}^\dagger \mathcal{L} U_{\text{gl}} = \Xi + \Theta$ splits into a gain/loss contribution,

$$\Xi \equiv U_{\text{gl}}^\dagger \mathcal{L} U_{\text{gl}}|_{J=0} = \text{diag}(-i\sqrt{2}\eta, i\sqrt{2}\eta, 0), \quad (19)$$

and an interactions/frequency shifts contribution,

$$\Theta = \begin{pmatrix} \frac{1}{2}J \cos(\phi) & -\frac{1}{2}J \cos(\phi) & \frac{J \sin(\phi)}{\sqrt{2}} \\ -\frac{1}{2}J \cos(\phi) & \frac{1}{2}J \cos(\phi) & \frac{J \sin(\phi)}{\sqrt{2}} \\ -\frac{J \sin(\phi)}{\sqrt{2}} & \frac{J \sin(\phi)}{\sqrt{2}} & -J \cos(\phi) \end{pmatrix}. \quad (20)$$

Equation (18) regroups gain and loss into effective sites a_l , a_- and a_g , revealing an effective gain-loss mirror plane with parity operation $\mathcal{P}_{\text{gl}}: a_g \leftrightarrow a_l$.

\mathcal{L}_{gl} respects $\mathcal{P}_{\text{gl}} \mathcal{T}$ symmetry for arbitrary flux, where $\mathcal{T}: i \mapsto -i$, $\mathcal{T}: \phi \mapsto -\phi$. The coupling topology, however, is flux-dependent (see text). In particular, when $\phi = 0$, the dynamical matrix reads:

$$\mathcal{L}_{\text{gl}}|_{\phi=0} = \begin{pmatrix} \frac{J}{2} - i\sqrt{2}\eta & -\frac{J}{2} & 0 \\ -\frac{J}{2} & \frac{J}{2} + i\sqrt{2}\eta & 0 \\ 0 & 0 & -J \end{pmatrix}, \quad (21)$$

that is, it leaves the mode a_- uncoupled from the remaining $\mathcal{P}_{\text{gl}} \mathcal{T}$ -symmetric dimer for a_g and a_l (see Fig. 4d, inset). Conversely, a linear trimer structure follows at $\phi = \pm\pi/2$, where the dynamical matrix reads:

$$\mathcal{L}_{\text{gl}}|_{\phi=\pm\pi/2} = \begin{pmatrix} -i\sqrt{2}\eta & 0 & \mp \frac{J}{\sqrt{2}} \\ 0 & i\sqrt{2}\eta & \pm \frac{J}{\sqrt{2}} \\ \mp \frac{J}{\sqrt{2}} & \pm \frac{J}{\sqrt{2}} & 0 \end{pmatrix}. \quad (22)$$

From equations (21), (22), we can directly observe that flux affects the nature of the arising exceptional points, which can be either second or third order. Note that while finite synthetic fluxes retain $\mathcal{P}_{\text{gl}} \mathcal{T}$ symmetry of \mathcal{L} , they break the mirror symmetry $\mathcal{P}_{12}: a_1 \leftrightarrow a_2$, affecting the localization transition above the exceptional point (see text, Extended Data Fig. 4). The full expressions for the eigenspectra and population dynamics that illustrate this behaviour can be found in Supplementary Information section IID, E.

Subdominant and non-Lorentzian spectral features in the squeezing dimer

In the thermomechanical noise spectra of the squeezing dimer in Fig. 2e, f, we expect narrow and broad, frequency-degenerate, resonances. We show this in the ideal squeezing dimer ($\gamma_i = \gamma$), the spectrum of which is obtained in a closed form using the relationship via the quantum regression theorem (Supplementary Information section IE),

$$S(\omega) = \langle \alpha^\dagger(\omega) \alpha(\omega) \rangle = \chi_m^\dagger(\omega) \mathcal{D} \chi_m(\omega), \quad (23)$$

with mechanical susceptibility matrix $\chi_m(\omega) = i/(\omega(1) - H_{SD})$ and diffusion matrix \mathcal{D} , given earlier. The noise spectrum of resonator $i \in \{1, 2\}$ is given by the diagonal element $S_{ii}(\omega)$. An explicit calculation for the squeezing dimer shows that even in the simplified limit of equal resonator bath occupations, $\bar{n}_i = \bar{n}$, the spectrum consists of four superimposed Lorentzian responses located at the real parts of the eigenfrequencies of \mathcal{H}_{SD} for $\Phi = \pi$, where two pairs of resonances split by $2J$ and

$$S_{ii}(\omega) \propto \gamma \sum_{\Omega=\pm J} \left(\frac{\bar{n}+1}{(\gamma+2\eta)^2 + 4(\omega-\Omega)^2} + \frac{\bar{n}}{(\gamma-2\eta)^2 + 4(\omega-\Omega)^2} \right). \quad (24)$$

From equation (24), it is apparent that the spectral weight in the rotating frame at $\pm J$ in the stable regime ($\gamma > 2\eta$) is concentrated in a dominant, narrow resonance with linewidth $\gamma - 2\eta$, on top of a heavily damped contribution with linewidth $\gamma + 2\eta$.

By contrast, the branch-cut topology mandated by the exceptional point at $\Phi = 0$ results in a non-Lorentzian thermal response. If $\Phi = 0$, the spectrum contains non-Lorentzian contributions

$$\begin{aligned} S_{ii}(\omega) &\propto \frac{2\gamma[(2\bar{n}+1)(\gamma^2 + 4(\eta^2 + J^2 + \omega^2)) - 4\gamma\eta]}{d(\omega)}, \\ d(\omega) &= 8\omega^2(\gamma^2 + 4(\eta^2 - J^2)) \\ &\quad + (\gamma^2 - 4(\eta^2 - J^2))^2 + 16\omega^4. \end{aligned} \quad (25)$$

Equation (25) reduces at the exceptional point ($J = \eta$) to the following expression, which shows directly a double-Lorentzian response.⁶³

$$S_{ii}(\omega) \propto \frac{\gamma(2\bar{n}+1)(2J^2 + \gamma^2/4 + \omega^2) - \gamma J}{(\gamma^2/4 + \omega^2)^2}. \quad (26)$$

This functional form implies deviations in the experimental linewidths in the vicinity of an exceptional point obtained from Lorentzian spectral fitting (Extended Data Fig. 2 and Supplementary Information section IIIA).

Sample design and fabrication

The device, shown in Extended Data Fig. 5a, was designed as a sliced photonic crystal nanobeam with two beam halves of different mass to create non-degenerate mechanical modes. The cavity was defined away from the beams' centres to optically access flexural modes with even as well as odd symmetries. The cavity is designed as a single-site defect, by locally varying hole pitch in the one-dimensional photonic crystal. This creates a cavity with considerable optical coupling to focused light normally incident from free space⁶⁴. It also results in a relatively large optical linewidth ($\kappa \approx 320$ GHz), ensuring that the cavity population responds linearly to thermal excitations (at the optimal detuning), such that nonlinear transduction⁶⁵ and detrimental reduction of the optical spring shift are not important. Devices were fabricated from a silicon-on-insulator substrate, with a 220-nm device layer and 3-μm buried oxide layer. A 50-nm layer of diluted hydrogen silsesquioxane resist (1:2 in methyl isobutyl ketone) was spin-coated, and electron-beam lithography (Raith Voyager) was used to write patterns on the sample.

After developing in tetramethylammonium hydroxide, an anisotropic etch of the exposed device layer was done using inductively coupled plasma–reactive ion etching with HBr and O₂ gases. The nanobeams were suspended in a wet etch of the underlying buried oxide layer with hydrofluoric acid followed by critical point drying.

Experimental set-up

A schematic of the experimental set-up is presented in Extended Data Fig. 5b. The sample was placed, with the devices rotated by 45° relative to the vertical polarization of the incoming light, in a vacuum chamber at room temperature at a pressure of 2×10^{-6} mbar. A tunable laser (Toptica CTL 1500) connected through a Thorlabs LN81S-FC intensity modulator was used as the drive laser (power incident on device P_{drive} up to 1.0 mW). A small part of the modulated drive laser light was split using a fibre-based beamsplitter and fed onto a fibre-coupled fast photodetector (New Focus 1811, d.c.-coupled) to monitor the drive signal. A second laser (New Focus TLB-6328 or Toptica CTL 1550), far detuned from the cavity resonance ($\omega_{\text{det}} - \omega_c \approx -2.5\kappa$), was used as the detection laser (power incident on device P_{det} = 2–4 mW). The lasers were combined on a fibre-based beam combiner and launched using a fibre collimator into the free-space set-up.

Control signals were generated by a lock-in amplifier (Zurich Instruments UHFLI). One output of the lock-in amplifier carried signals to generate interactions, and the other output carried coherent excitation signals. Both outputs were routed through individual radio frequency (RF) switches (Mini-Circuits ZYSWA-2-50DR+), combined, amplified (Mini-Circuits ZHL-32A+ with 9 dB attenuation) and connected to the RF port of the intensity modulator to drive and modulate the nanobeam mechanics. For time-resolved experiments, a synchronized two-channel signal generator (Siglent SDG1062X) was used to generate pulses to actuate both RF switches and trigger the lock-in amplifier acquisition.

Reflected detection laser light that interacted with the cavity was filtered using a cross-polarized detection scheme, fibre-coupled, separated from the drive laser using a tunable bandpass filter (DiCon), and detected on a fast, low-noise photodetector (New Focus 1811, a.c.-coupled). Intensity modulations of the detection laser encoding resonator displacements were analysed using the lock-in amplifier.

To generate a feedback signal, the electronic displacement signal was split and filtered using a digital signal processor (DSP, RedPitaya STEMlab 125-14) that implemented a configurable electronic bandpass filter with tunable gain and phase shift (using the PyRPL suite). The output of the DSP was combined with the control signals just before the RF amplifier.

Experimental procedure

Resonator characterization. The intrinsic, optically unmodified resonator frequencies $\tilde{\omega}_i$ and linewidths $\tilde{\gamma}_i$ were obtained by switching off the drive laser and recording a thermomechanical spectrum with the detection laser. A power sweep of the detection laser verified that the detection laser did not induce a noticeable optical shift in frequency or linewidth. The vacuum optomechanical coupling for the resonators $g_0^{(i)}$ is estimated from nonlinear transduction⁶⁵, with fitted values $g_0^{(i)}/(2\pi) = \{5.30 \pm 0.14, 5.86 \pm 0.17, 3.29 \pm 0.30, 3.12 \pm 0.89\}$ MHz (mean \pm Std from fitting uncertainty, where Std denotes the standard deviation; see section 'Error estimation') for the four resonators, respectively. The linewidth of the optical cavity was estimated from the detuning dependence of the spring shift (Extended Data Fig. 6).

To compensate for variations in incoupling and outcoupling efficiency, caused by position drift of the sample stage, the following reference procedure was performed immediately before every experiment: A thermomechanical spectrum was taken to obtain the spring-shifted resonator frequencies ω_i , linewidths γ_i , and root-mean-square (r.m.s.) displacement voltage levels $z_{\text{rms},i}$. From the r.m.s. level, the displacement voltage corresponding to a single phonon was calculated using $z_{\text{ph},i}^2 = z_{\text{rms},i}^2 / (\bar{n}_i \tilde{\gamma}_i / \gamma_i)$, where $\bar{n}_i = k_B T / \hbar \omega_i$ is the

Article

occupation of the resonator's phonon bath at room temperature $T = 295$ K. The ratio $\tilde{\gamma}_i/\gamma_i$ compensates for thermo-optically induced dynamical backaction⁶⁶ that changes the effective bath temperatures²⁹ (see Extended Data Fig. 6d). Control over dynamical backaction is also used in the squeezing dimer experiments to equalize loss rates for the two resonators. Fine-tuning the laser intensity enables us to match the two linewidths of modes 3 and 4 specifically, as they exhibit different scaling with mean photon number.

Calibration of control signals. To find the linear operation point of the intensity modulator, a sinusoidal modulation voltage was applied while sweeping its amplitude and monitoring the modulated drive laser. The intensity modulator bias voltage was varied to minimize the variation in d.c. transmission as a function of modulation amplitude. To compensate for frequency-dependent transmission in the RF chain, the relation between control signal voltage amplitude V_m and modulation depth c_m was measured individually for every tone using the d.c.-coupled modulation monitor detector.

For the beamsplitter trimer experiments in Fig. 1, a linear relation between modulation amplitude V_m and the beamsplitter coupling J_{ij} induced by sinusoidal modulation at $\omega_m = \omega_i - \omega_j$, $i \neq j$ was established by sweeping V_m , recording thermomechanical spectra of resonators i and j and fitting the frequency splitting of the hybridized modes.

Spectral estimation of the strength of a squeezing interaction is less precise, owing to the spectral superposition of gain and loss (see Extended Data Fig. 7). Therefore, in the other experiments, the squeezing and beamsplitter interaction strengths $\eta_{ij}J_{ij}$ induced by a sinusoidal drive laser modulation at frequency $\omega_m = \omega_i \pm \omega_j$ (for $i \neq j$ or $i = j$) and modulation depth c_m were obtained using the relationship

$$\{\eta_{ij}, J_{ij}\} = c_m \sqrt{\delta\omega_i \delta\omega_j} / 2, \quad (27)$$

where $\delta\omega_i = \omega_i - \tilde{\omega}_i$ is the optical spring shift of resonator i . Note that $\delta\omega_i$ and $\delta\omega_j$ always have the same sign. Using this relation avoids the need to know the photon–phonon coupling rates $g_0^{(i)}$ and cavity incoupling efficiency precisely. To verify, the effective beamsplitter interaction strength obtained above was compared to the frequency splitting observed in thermomechanical spectra for a sweep of the modulation depth c_m (see Extended Data Fig. 1). From this, a difference between calculated and actual interaction strength of about 10% was obtained, presumably owing to a difference in the modulation detector sensitivity at d.c. or a limited modulation range of the intensity modulator. This difference was applied as a correction factor to all calculated interaction strengths.

For the squeezing dimer experiments (Figs. 2, 3), performed with high modulation depths $c_m > 0.5$, a relation between c_m and V_m was established using the first-order Bessel function $J_1(x)$, derived from a Jacobi–Anger expansion of the intensity modulator cosine response. In addition, a linear correction on the scaling of the beamsplitter coupling J was obtained by fitting the linear frequency splitting for $\Phi = \pi$ (as shown in Fig. 3b) as a function of c_m .

In the beamsplitter trimer experiments, the flux offset $\Phi_0 = \varphi_{23} + \varphi_{31}$ was obtained by extracting eigenfrequencies from thermomechanical spectra as a function of φ_{12} and fitting those to the eigenfrequencies $\epsilon_k = 2/\cos((2\pi k + \Phi)/3)$ of the Hamiltonian H_{B3T} in equation (1) indexed by $k = \{-1, 0, 1\}$, where $\Phi = \Phi_0 + \varphi_{12}$. In the other experiments, to circumvent spectral estimation of the flux and to facilitate the analysis of (anti)squeezed quadratures, the phases of the control tones are referred to an effective time origin internal to the lock-in amplifier, which enables us to define a deterministic gauge in which the modulation phases are set and the response is analysed. This method was verified by applying it to the beamsplitter trimer and comparing it to the flux offset fitting method outlined above.

To realize the equalization of dissipation rates in the singly conjugated trimer experiments, a feedback signal was obtained by filtering the electronic displacement signal around each resonator's frequency ω_i in parallel (second-order filter half-width at half-maximum 78 kHz), applying individual gains and phase shifts, and digitally combining the filtered signals. For each mode, the optimal feedback phase shift was found by taking thermomechanical spectra using fixed feedback gain for a full sweep of the phase shift, fitting the extracted linewidths with a sinusoidal variation and selecting the shift with the largest change in linewidth (see Extended Data Fig. 8). Subsequently, for the optimal phase shift, thermomechanical spectra were taken for various settings of the feedback gain and a linear relation was fitted between gain and extracted linewidths.

Analysis of the displacement signal. The electronic displacement signal was demodulated in parallel at each resonator's frequency ω_i using electronic local oscillators internal to the lock-in amplifier that are referenced to the same time origin as the control tones. For each resonator, the demodulated in-phase (I_i) and quadrature (Q_i) components were filtered (third-order low-pass filter, 3 dB bandwidth 50 kHz) and combined into a complex amplitude $z_i(t) = I_i(t) + iQ_i(t)$ that is formally equivalent to the resonator amplitude in the rotating frame. The complex amplitudes of all resonators involved were acquired simultaneously, at a rate $(50\text{--}500) \times 10^3$ samples per second, depending on the experiment. These complex time traces were normalized using the signal levels obtained in the reference procedure described earlier and were either (i) analysed directly to yield phase-space distributions; (ii) averaged coherently, that is, $\langle z_i(t) \rangle$; or (iii) Fourier transformed (Hann windowing function), squared and averaged to yield energy spectral densities (ESDs). In the last case, the low-pass filter was compensated for by dividing spectral densities by the filter frequency response. Time-resolved experiments were averaged over 1,000 runs.

The total signal delay through the set-up, from the lock-in amplifier control outputs via the sample to the lock-in amplifier input, was determined by driving each of the resonators and measuring the coherent response (see Extended Data Fig. 9). The phase offset α_i between the drive tone and coherent response of resonator i was extracted and fitted linearly against the resonator frequencies ω_i . The fitted delay was used to relate the quadratures of the demodulated amplitudes $z_i(t)$ to those defined by the control tones. This relation was verified for resonators 3 and 4 (that is, the modes that participate in the squeezing dimer) by turning on a single-mode squeezing interaction, recording a thermomechanical time trace, constructing a phase-space distribution and fitting the angle of the squeezed and anti-squeezed principal quadrature axes (see Extended Data Fig. 7).

Error estimation

The error on fitted values such as frequencies and linewidths originates from multiple sources. Error bars in plots indicate $\pm 2\sigma$, that is, a 95% confidence interval for a normal distribution.

The stability of the interaction strength over typical measurement timescales (-100 s) is controlled by the stability of the drive laser power (relative standard deviation $\sigma_{P_{\text{drive}}}/P_{\text{drive}} \approx 2 \times 10^{-3}$) entering equation (27) through $\delta\omega_i$ and the stability of the modulation depth (relative standard deviation $\sigma_{c_m}/c_m \approx 10^{-3}$).

In addition, jitter of the spring shift $\delta\omega_i$ due to variations in drive laser power and incoupling efficiency controls the detuning of the control signals. For resonators with comparable $g_0^{(i)}$ (that is, resonators 1, 2 and resonators 3, 4), the effect of detuning jitter on beamsplitter interactions—which depend only on their frequency difference—is reduced. To estimate the effect of detuning jitter on the effective linewidth change induced by squeezing interactions, Monte Carlo integration is used.

Finally, the fit uncertainty is estimated using a numerical approximation of the Jacobian matrix.

The standard error of the experimental (co)variances $\sigma(A, B)$ of quadratures A and B is estimated using the statistical relationship

$$\text{Std}(\sigma(A, B)^2) \approx \sqrt{\frac{1}{n-1}(\sigma(A, B)^4 + \sigma(A, A)^2\sigma(B, B)^2)},$$

Here, n is the number of thermally independent measurement points, given by $n = T\gamma_i/2$, where $T = 0.3$ s is the duration of the measurement record and γ_i is the dissipation rate of the resonator involved.

Data availability

The data in this study are available from the Zenodo repository at <https://doi.org/10.5281/zenodo.6320519>.

55. Bender, C. M. & Boettcher, S. Real spectra in non-Hermitian Hamiltonians having \mathcal{PT} symmetry. *Phys. Rev. Lett.* **80**, 5243 (1998).
56. Ruter, C. E. et al. Observation of parity-time symmetry in optics. *Nat. Phys.* **6**, 192–195 (2010).
57. Ornigotti, M. & Szameit, A. Quasi \mathcal{PT} -symmetry in passive photonic lattices. *J. Opt.* **16**, 065501 (2014).
58. Li, H., Mekawy, A., Krasnok, A. & Alù, A. Virtual parity-time symmetry. *Phys. Rev. Lett.* **124**, 193901 (2020).
59. Heiss, W. D. The physics of exceptional points. *J. Phys. A* **45**, 444016 (2012).
60. Moiseyev, N. *Non-Hermitian Quantum Mechanics* (Cambridge Univ. Press, 2011).
61. Koch, J., Houck, A. A., Hur, K. L. & Girvin, S. M. Time-reversal symmetry breaking in circuit-QED-based photon lattices. *Phys. Rev. A* **82**, 043811 (2010).
62. Ranzani, L. & Aumentado, J. Graph-based analysis of nonreciprocity in coupled-mode systems. *New J. Phys.* **17**, 023024 (2015).
63. Takata, K. et al. Observing exceptional point degeneracy of radiation with electrically pumped photonic crystal coupled-nanocavity lasers. *Optica* **8**, 184 (2021).
64. Leijssen, R. & Verhagen, E. Strong optomechanical interactions in a sliced photonic crystal nanobeam. *Sci Rep.* **5**, 15974 (2015).
65. Leijssen, R., La Gala, G. R., Freisem, L., Muñonen, J. T. & Verhagen, E. Nonlinear cavity optomechanics with nanomechanical thermal fluctuations. *Nat. Commun.* **8**, 16024 (2017).
66. Hauer, B. D., Clark, T. J., Kim, P. H., Doolin, C. & Davis, J. P. Dueling dynamical backaction in a cryogenic optomechanical cavity. *Phys. Rev. A* **99**, 053803 (2019).
67. Frimmer, M. & Novotny, L. The classical Bloch equations. *Am. J. Phys.* **82**, 947–954 (2014).

Acknowledgements We thank C. Wanjura, A. Nunnenkamp and M. Brunelli for discussions, and M. Serra-Garcia, S. Rodriguez, F. Koenderink and O. Zilberberg for critical reading of the manuscript. This work is part of the research programme of the Netherlands Organisation for Scientific Research (NWO). We acknowledge support from the European Research Council (ERC starting grant no. 759644-TOPP) and the European Union's Horizon 2020 research and innovation programme under grant agreement no. 732894 (FET Proactive HOT). J.d.P. acknowledges financial support from the ETH Fellowship programme (grant no. 20-2 FEL-66).

Author contributions J.d.P. developed the theoretical framework. J.J.S. fabricated the sample, performed the experiments, analysed the data and aided in constructing the theoretical approach. E.V. conceived and supervised the project. All authors contributed to the interpretation of results and writing of the manuscript.

Competing interests The authors declare no competing interests.

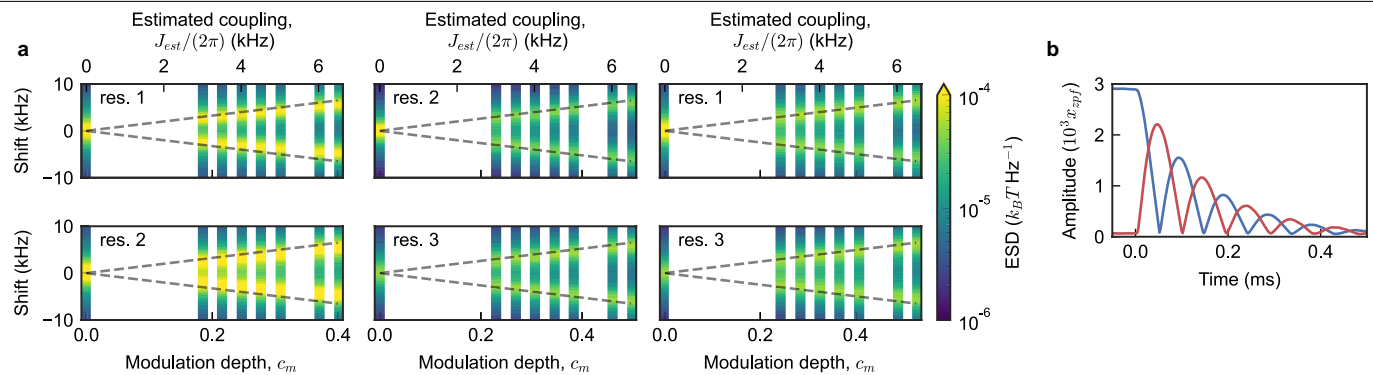
Additional information

Supplementary information The online version contains supplementary material available at <https://doi.org/10.1038/s41586-022-04609-0>.

Correspondence and requests for materials should be addressed to Javier del Pino or Ewold Verhagen.

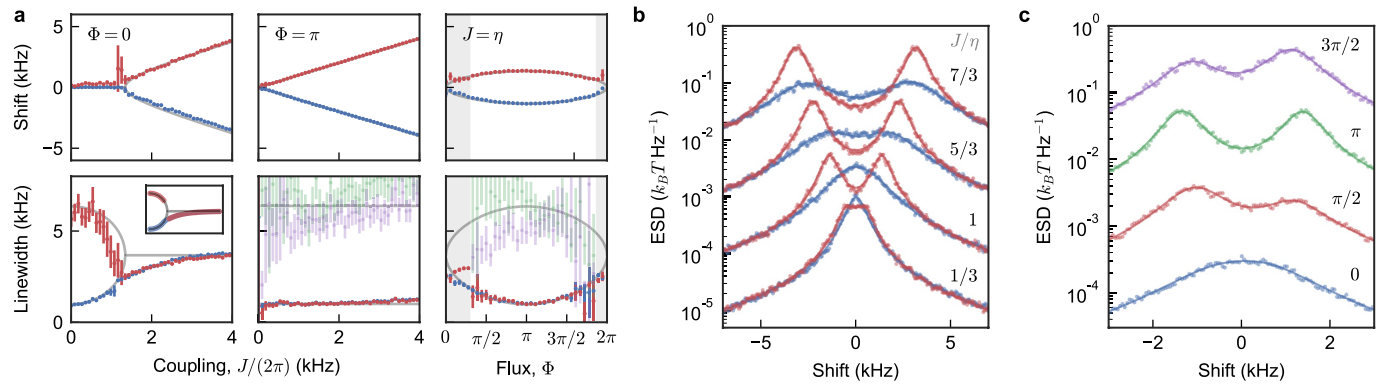
Peer review information *Nature* thanks the anonymous reviewers for their contribution to the peer review of this work. Peer reviewer reports are available.

Reprints and permissions information is available at <http://www.nature.com/reprints>.


Extended Data Fig. 1 | Estimation of beamsplitter interaction strengths.

a, Mode splitting induced by a beamsplitter interaction observed in thermomechanical spectra. Each column corresponds to a beamsplitter interaction induced between a pair of resonators $i \leftrightarrow j$ (left: $1 \leftrightarrow 2$, middle: $2 \leftrightarrow 3$, right: $1 \leftrightarrow 3$) by a single drive laser modulation at frequency $\Delta\omega_y = \omega_i - \omega_j$, where ω_{ij} is the frequency of resonator i,j . Thermomechanical spectra (top row: resonator i , bottom row: resonator j) are recorded for increasing modulation depth c_m . The linear relationship $J_{est} = c_m \sqrt{\delta\omega_i \delta\omega_j} / 2$ is used to estimate the coupling strength J_{est} (top axis) from c_m , where $\delta\omega_{ij}$ is the optical spring shift of mode i,j . The estimated mode splitting (dashed) is slightly larger than observed, presumably due to frequency-dependent transduction (at d.c. and frequency $\Delta\omega_y$) in the measurement of c_m . The difference is quantified by extracting Lorentzian peak frequencies from the spectra and subsequently fitting those linearly against modulation depth, and results in an observed mode splitting slope that is 78%, 90% and 90% of the estimated slope,

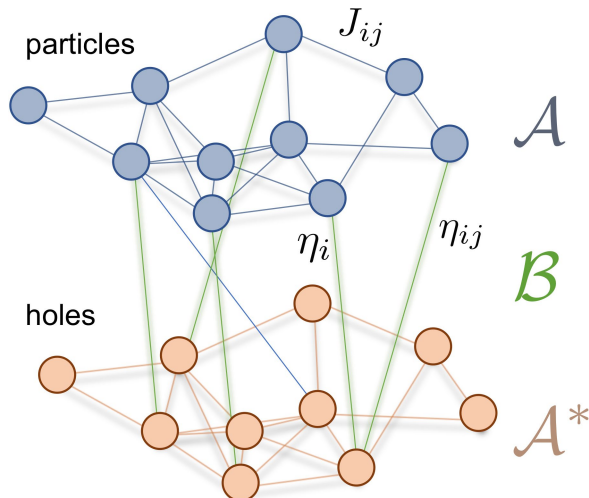
respectively. The average estimation offset of 86% is applied to all (beamsplitter and squeezing) interaction strength calculations in our experiments. **b**, Time evolution of the coherent amplitude (in units of their zero-point fluctuations x_{zpf}) of a pair of resonators (1, blue and 2, red) coupled through a beamsplitter interaction (strength $/ (2\pi) = 5$ kHz). Resonator 1 is initially (time $t < 0$) driven to a high-amplitude steady state by a coherent drive laser modulation. At $t = 0$, the drive is switched off and the interaction is switched on. Rabi oscillations induced by the coupling interaction are observed, where energy is transferred back and forth between the resonators until the coherent energy in the resonators is dissipated. These dynamics illustrate the possibility for a transfer scheme in the strong-coupling regime where couplings are interrupted after a Rabi semi-cycle, that is, a time $t_\pi = \pi / (2J)$. The energy transfer efficiency for this process can be calculated⁶⁷ to be ~64% for corresponding parameters and 70% for the coupling rates presented in Fig. 1.



Extended Data Fig. 2 | Frequency and linewidth modulation in the squeezing dimer. **a**, Experimental resonance frequencies (top) and linewidths (bottom) obtained by fitting a superposition of Lorentzian lineshapes to the thermomechanical spectra in Fig. 3c, d. Grey curves indicate theoretical values of $\text{Re}(e)$ (top) and $\text{Im}(e)$ (bottom). Two peaks were fitted to the spectra for $\Phi = 0$ (left), as for that flux both eigenvalues are expected to be doubly degenerate for all J . The observed branching of frequencies and linewidths is characteristic of an exceptional point. Four peaks were instead fitted for $\Phi = \pi$ (middle), where the exceptional-point behaviour completely vanishes, and spectra are fitted well with a combination of broad and narrow peaks at two frequencies.

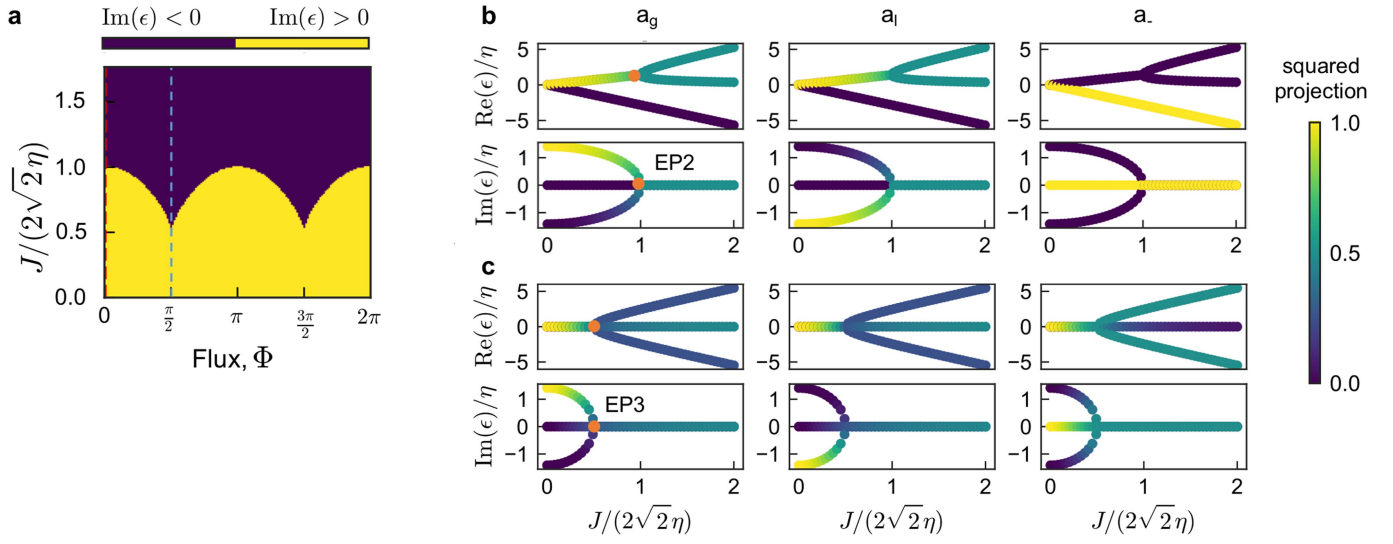
When varying flux in the rightmost panel, the grey shaded areas depict the regions near $\Phi = 0, \pi$ where a fit of two peaks provided better results than a fit of four. Note that near the exceptional point, the non-Lorentzian nature of the spectrum causes the fitted values of the Lorentzian linewidths to deviate from the theoretical $\text{Im}(e)$. This origin of the deviation is confirmed by applying the same fit procedure to theoretically predicted spectra (inset, bottom left), which shows the same deviation. Error estimation is described in Methods section ‘Error estimation’. **b**, Thermomechanical spectra for several values of J/η , for $\Phi = 0$ (blue) and $\Phi = \pi$ (red). Solid lines show Lorentzian fits. **c**, As in **b**, but for different values of Φ at $J = \eta$.

Article



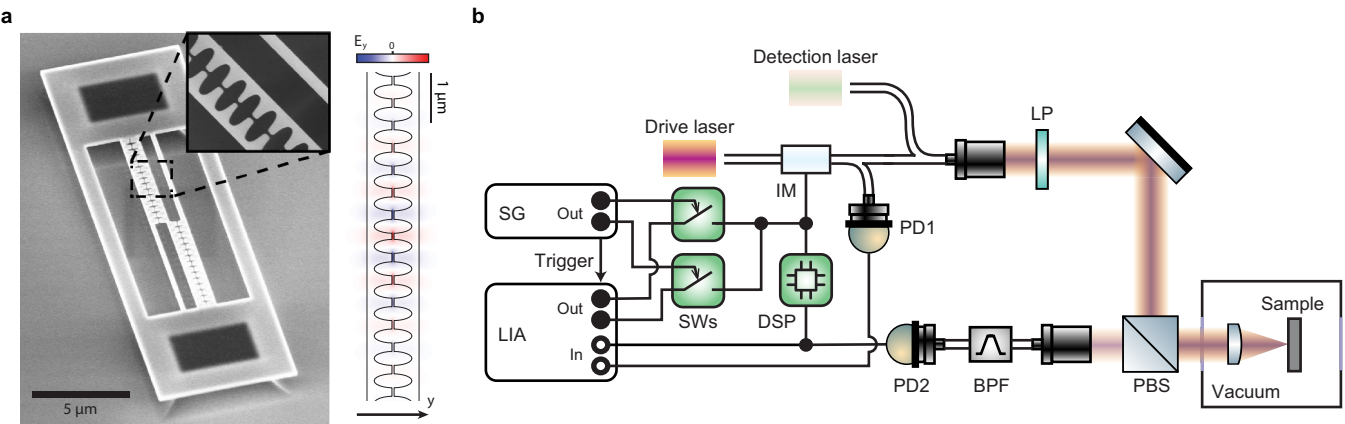
Extended Data Fig. 3 | Network graph representation of general quadratic

Hamiltonians. Schematic of an arbitrary Hamiltonian matrix \mathcal{H} , acting on a Nambu-like vector $\alpha = (a_1, a_2, \dots, a_N, a_1^\dagger, a_2^\dagger, \dots, a_N^\dagger)$. Particle annihilation (hole creation) operators, a_i , are represented by blue nodes, and hole annihilation (particle creation) operators are represented by orange nodes. \mathcal{H} includes excitation-conserving interactions (matrix \mathcal{A}), which link particle operators (for example, terms $\mathcal{A}_{ij}a_i^\dagger a_j$) and hole operators (for example, terms $\mathcal{A}_{ij}^*a_i a_j^\dagger$). Squeezing interactions (with complex amplitude matrix \mathcal{B}) contain pairs $\mathcal{B}_{ij}a_i^\dagger a_j^\dagger$ that can be visualized to either annihilate two particles i, j or to annihilate a particle in i and create hole in j , hence the connection between particle and hole networks (green). *Mutatis mutandis*, terms $\mathcal{B}_{ij}^*a_i a_j$ can be similarly visualized.



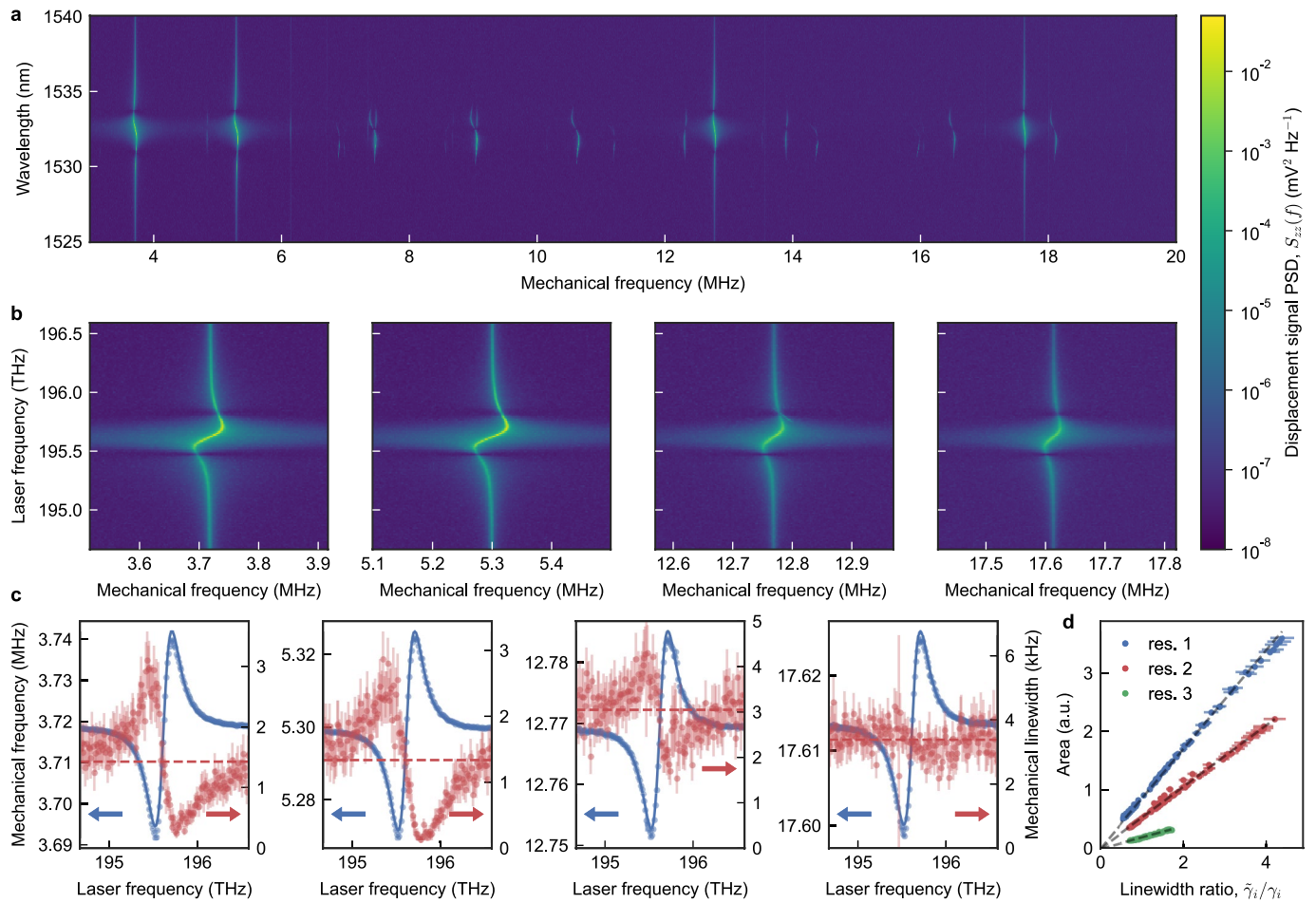
Extended Data Fig. 4 | Calculated eigenstates of the a_1, a_2, a_3^\dagger loop in the singly conjugated trimer studied in Fig. 4. **a**, Phase diagram for the imaginary part of the eigenfrequencies, showing the stability-to-instability boundary in ξ - Φ space, where $\xi = J/(2\sqrt{2}\eta)$ and $\gamma_i = 0$. Such boundary is associated with a second-order exceptional contour. **b**, Cuts of the eigenfrequency Riemann surfaces along $\Phi = 0$, shown as a red dashed trajectory in the phase diagram, as a function of the ratio $\xi = J/(2\sqrt{2}\eta)$. The squared weights of the $J = 0$ eigenstates in the full eigenvectors are shown in the colour scale. The weights are calculated from the symplectic projections (Σ_z product) on the gainy/lossy

combinations a_g, a_1 and the passive mode a_- . A second-order exceptional point (denoted EP2), found for $J = 2\sqrt{2}\eta$, is highlighted. As $J < 2\sqrt{2}\eta$, \mathcal{P}_{gT} symmetry is spontaneously broken, inducing eigenstate localization. The antisymmetric 1-2 mode a_- is detached from this mechanism and remains uncoupled. Real and imaginary parts are rescaled by η . **c**, As in **b**, but along the cut $\Phi = \pi/2$ (corresponding to the blue dashed line in **a**, which shows the third-order exceptional point (EP3) at $J = \sqrt{2}\eta$). The \mathcal{P}_{gT} -symmetry broken states are now hybrid combinations of a_g/a_+ and a_+/a_- modes. Such combinations break \mathcal{P}_{12T} symmetry as well, as explained in the text.



Extended Data Fig. 5 | Experimental set-up. **a**, Electron micrograph (left, tilt 45°; inset, top view) showing a device as used in our experiments. In the top silicon device layer (thickness 220 nm), three suspended beams are defined with teeth separated by a narrow slit (~50 nm). Between each outer beam and the central beam, a photonic crystal cavity is defined that hosts an optical mode (right, simulated electric field y component, E_y). The mode's energy is strongly confined to the narrow slits, inducing large parametric interaction with flexural mechanical resonances of the two beams. The cavity's off-centre position ensures coupling to both even and odd resonances. In the presented experiments, we only use one of the two cavities. The widths of the outer beams' straight sections are intentionally made unequal, such that the mechanical resonances of all beams are detuned. The top layer is supported by

pedestals etched out in the buried silicon oxide layer. **b**, Schematic of the experimental set-up. The ultrahigh-frequency lock-in amplifier (LIA) ports serve to (Out) drive the intensity modulator through an amplification stage (not shown) and to (In) analyse intensity modulations of the drive laser (for calibration) and detection laser. For time-resolved measurements, the signal generator (SG) is programmed to (Out) actuate the drive signal switches and trigger the lock-in amplifier acquisition. The digital signal processor (DSP) optionally generates a feedback signal to modify resonator damping rates. BPF, optical bandpass filter; IM, intensity modulator; LP, linear polarizer; PBS, polarizing beamsplitter; PD1, PD2, photodiodes; SWs, microwave switches.



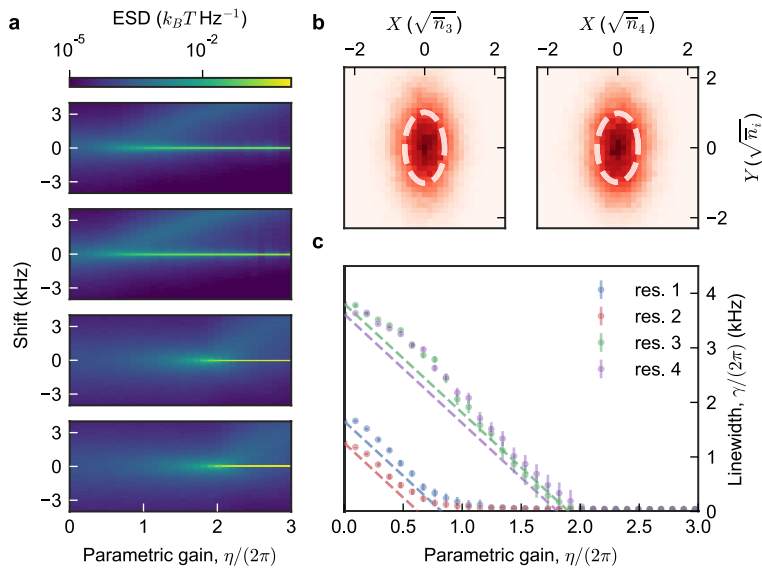
Extended Data Fig. 6 | Optical spring shift and opto-thermal backaction.

a, Thermomechanical noise spectra of the first few mechanical modes imprinted on an unmodulated single drive/detection laser, as the laser's frequency (ω_L) is swept across the cavity resonance. The four most intense peaks around frequencies $\omega_i/(2\pi) \approx \{3.7, 5.3, 12.8, 17.6\}$ MHz correspond to flexural modes (labelled i) of the individual beam halves and show frequency-tuning characteristic to the optical spring effect, and the other peaks represent nonlinearly transduced harmonics of those modes.⁶⁵. PSD, power spectral density.

b, Magnification of the PSD of the first four resonators.

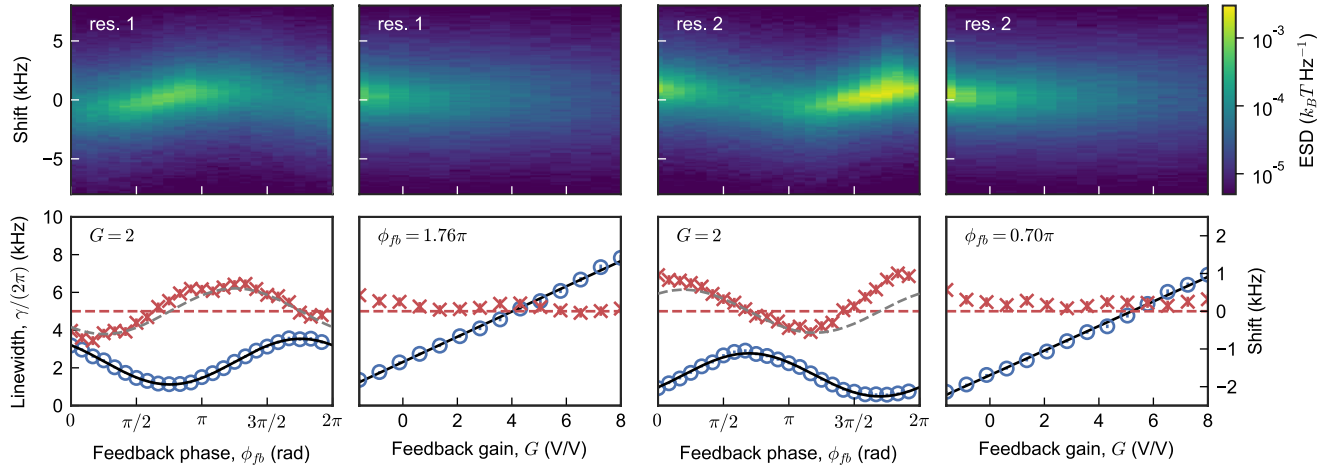
c, From the spectra in **b**, resonance frequencies ω_i (blue circles) and linewidths γ_i (red circles) are extracted. The resonance frequencies are fitted using the standard optical spring model (solid blue). Across all resonators, we find agreement in the fitted cavity resonance $\omega_c/(2\pi) = 195.62$ THz and linewidth $\kappa/(2\pi) = 320$ GHz (Q factor, $Q \approx 600$). The small sideband resolution $\omega_i/\kappa \approx 10^{-5}$ suggests very little change in linewidth due to dynamical cavity

backaction (dashed red). The linewidth modulations we observe suggest the presence of an opto-thermal retardation effect⁶⁶. Displayed errors correspond to fit uncertainty, smaller than plot markers on the fitted frequencies (Methods section 'Error estimation'). On each panel, blue/red colour-coded arrows indicate the y scale for each plotted quantity. **d**, Drive laser frequency sweep, now using a separate, fixed-frequency, far-detuned detection laser. The fixed transduction of mechanical motion onto this detection laser allows a comparison of resonance peak area $A_i(\omega_L)$ versus linewidth $\gamma_i(\omega_L)$ as the drive laser frequency ω_L is varied (a.u., arbitrary units). The resonance peak area of mode i is proportional to the variance $\langle X_i^2 \rangle$ of its displacement X_i , which is proportional to its temperature T_i . Dynamical backaction modifies the effective mode temperature through $T_i = T_0(\tilde{\gamma}_i/\gamma_i)$ (ref. ²⁹), where T_0 is the initial temperature and $\tilde{\gamma}_i$ is the mode's intrinsic linewidth, determined by switching off the drive laser. Our data are well explained by linear fits of $A_i(\omega_L)$ versus $\tilde{\gamma}_i/\gamma_i(\omega_L)$ (dashed), confirming the effective temperature model.



Extended Data Fig. 7 | Single-mode squeezing and linewidth modulation by parametric driving. **a**, Parametric gain induced by a single-mode squeezing interaction observed in thermomechanical spectra. Each row corresponds to a separate experiment where resonator i (1 through 4) is subjected to a single-mode squeezing interaction of strength η . As η is increased, the resonance transitions from the broad intrinsic linewidth to a narrow parametric resonance. **b**, The phase-space distribution of the thermal fluctuations of resonator i (left: 3; right: 4) subject to a single-mode squeezing interaction of strength $\eta/(2\pi) = 1 \text{ kHz}$ with squeezing angle $\theta = \pi/2$ reveals a squeezed (anti-squeezed) quadrature $X(Y)$, measured in units of the thermal equilibrium amplitude $\sqrt{\bar{n}_i}$, are referenced using the propagation delay (Methods). **c**, Fitted Lorentzian full-width at half-maximum linewidths of the resonances shown in **a**. Even though a

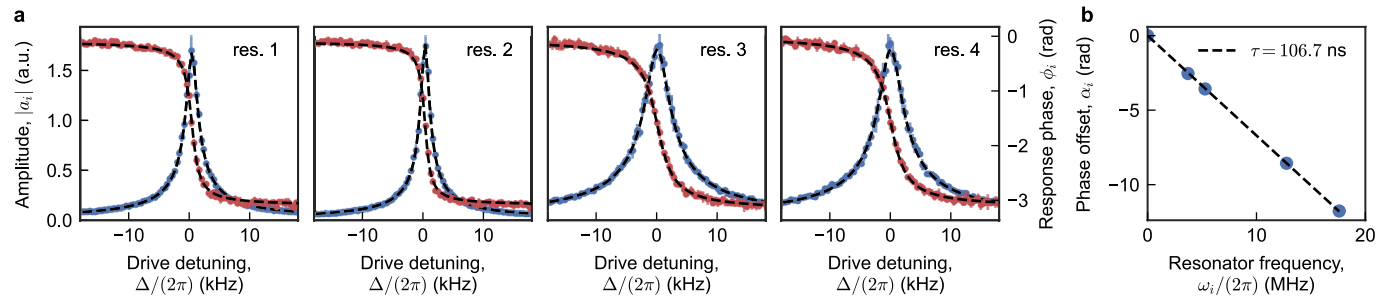
superposition of two degenerate resonances is expected—a broadened resonance of the anti-squeezed quadrature and a narrowed resonance of the squeezed quadrature—only a single one can be successfully fitted in each spectrum. This reflects the fact that the highly populated narrowed resonance dominates the broadened resonance. As the parametric gain η is increased, each resonator's squeezed quadrature linewidth is expected to decrease by $\Delta\gamma = -2\eta$ (dashed lines), until parametric threshold is reached at $\eta = \gamma_i/2$, where γ_i is the intrinsic linewidth of resonator i . The fitted linewidths follow the expected trend quite closely for intermediate η , whereas for lower η the narrow resonance is presumably not yet fully dominant and for larger η high-amplitude nonlinear effects are prominent. Error bars correspond to the fit uncertainty, and are smaller than the symbol size in most points (Methods section ‘Error estimation’).



Extended Data Fig. 8 | Damping rate adjustment by feedback. Resonator thermomechanical spectra (top row) and fitted full-width half-maximum linewidths (bottom row) adjusted by feeding back electronically filtered and phase-shifted resonator displacement signals onto the drive laser modulation (left two columns, resonator 1; right two columns, resonator 2). The resonator linewidth (circles) and frequency shift (crosses) vary sinusoidally with the feedback phase ϕ_{fb} (odd columns). By fitting the linewidth variation (solid black), the optimal phase shift to increase the damping rate is selected. The

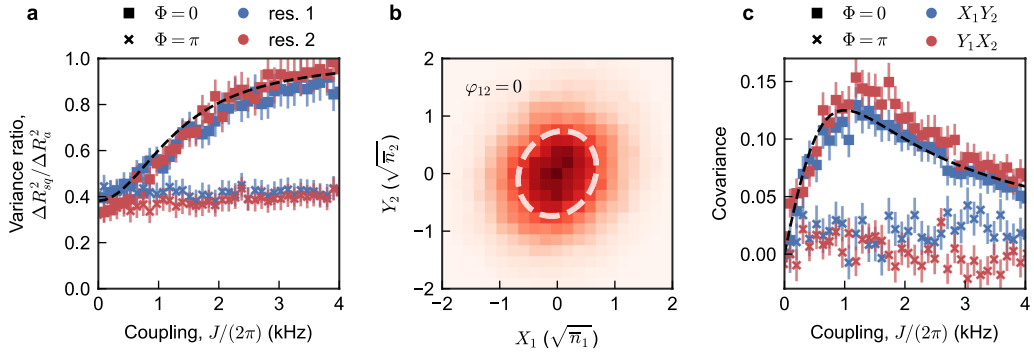
frequency variation (dashed grey) expected from the fitted linewidth modulation, relative to the resonator frequency with feedback off (dashed red), lags by $\pi/2$ radians. For the optimal feedback phase shift, an increase in linewidth is observed for increasing gain G , whereas the resonator frequency remains unaffected (even columns). The slope of the linear fit (solid black) can be used when setting a resonator's linewidth to a desired value. Error bars reflect the fit uncertainty and control parameter stability, and are typically smaller than the plot marker size (Methods section 'Error estimation').

Article



Extended Data Fig. 9 | Resonator coherent response. **a**, Amplitude $|a_i|$ (blue, left axis) and phase ϕ_i (red, right axis) of the complex response $a_i(\Delta) = e^{i(\phi_i(\Delta)+\alpha_i)}|a_i(\Delta)|$ of resonators 1 through 4 (resonance frequencies ω_i) to a drive laser modulation at a frequency ω_d close to resonance (drive detuning $\Delta = \omega_d - \omega_i$). α_i is the phase offset due to signal delay through the set-up. A Lorentzian response $a_i = e^{ia_i}A_i \frac{\gamma_i/2}{i\gamma_i/2 - \Delta}$ is fitted to the data (dashed). **b**, Phase

offset α_i versus resonance frequency $\omega_i/(2\pi)$. A linear fit (dashed) of $\alpha_i = -\omega_i\tau$ implies a signal delay $\tau = 106.7$ ns. Error bars in **a** reflect the spread in repeated measurement, whereas the error bars in **b** correspond to fit uncertainty and are smaller than the symbol size (Methods section ‘Error estimation’). a.u., arbitrary units.



Extended Data Fig. 10 | Tunable single-mode and effective two-mode squeezing in the squeezing dimer. **a**, Intra-resonator squeezing as a function of the beamsplitter coupling J . Two values $\Phi = 0, \pi$ of the flux are shown for equal single-mode squeezing strengths $\eta_1 = \eta_2 = 0.5$ kHz. The level of single-mode squeezing is expressed by the ratio of the smallest (ΔR_{sq}^2) and largest (ΔR_a^2) eigenvalues of the covariance matrix of the quadrature amplitudes recorded for each resonator. These eigenvalues indicate the amplitude variance along the squeezed and anti-squeezed principal quadrature components, respectively. For $\Phi = \pi$, where the squeezed (anti-squeezed) quadratures X_i (Y_i) of both resonators are coupled (see Fig. 2d), the slight initial imbalance in variance ratio is reduced as J increases while the value of the variance ratio remains low. By contrast, for $\Phi = 0$ —when the squeezed quadrature X_i in one resonator is coupled to the anti-squeezed quadrature Y_j in the other—we observe cancellation of single-mode squeezing as the variance ratio tends to 1 with increasing J . This agrees well with theory (dashed line), where for simplicity we have assumed equal dissipation rates $\bar{\gamma} = 2.2$ kHz equal to the average of the experimental losses $\gamma_i = \{2.6, 1.9\}$ kHz, as well as equal bath occupations.

Owing to dynamical (optothermal) backaction, for this particular experiment the effective bath occupations $\bar{n}_1 \approx \bar{n}_2$ only differed by a few per cent. **b**, Two-mode squeezing observed in the cross-resonator amplitude distribution of quadratures X_1 and Y_2 for $\Phi = 0, J = 3.5$ kHz and $\eta_1 = \eta_2 = 0.5$ kHz. The dashed ellipse depicts the standard deviation of the principal components of the quadrature covariance matrix and shows positive correlations between X_1 and Y_2 ($\text{covariance } \sigma(X_1, Y_2) = 0.08$). **c**, Covariance of the coupled quadrature pairs X_1Y_2 and Y_1X_2 as a function of J , with $\eta_1 = \eta_2 = 0.5$ kHz. No correlations are found for flux $\Phi = \pi$, when single-mode squeezing is strongest and independent of J (compare with **a**). However, for $\Phi = 0$, positive correlations $\sigma(X_1, Y_2), \sigma(Y_1, X_2) > 0$ are found when J is increased, as predicted by theory (dashed line). A trade-off between the squeezing axes rotation towards the standard two-mode squeezing limit and the decrease in the overall squeezing level as J is increased leads to a maximum covariance (although not optimal squeezing level for the rotated quadratures) at a coupling J_{opt} . For the simple theory model with equal dissipation and bath occupation that we use it is given by $J_{\text{opt}}^2 = (\bar{\gamma}^2 - 4\eta^2)/4$. Error bars in **a** and **c** reflect statistical uncertainty and control parameter stability (Methods section ‘Error estimation’).